

Salvadore Dali (1983): *The Swallowtail* (Oil on canvas, 73 x 92,2 cm). This is Dali's last work and belongs to the series of catastrophe paintings.

SIMPLE CLIMATE MODELS*

Klaus Fraedrich

Abstract. Climate modelling strategies are demonstrated by toy models of the greenhouse planet, the atmosphere, and the ocean. A minimum energy balance model of the greenhouse provides the setting for a review on the construction and analysis of climate systems, which are simple and noisy. Two prominent climate compartments follow; these are the mid-latitude atmosphere and the wind-driven ocean, which are also subjected to stochastic forcing. The atmosphere's dynamics is derived analytically for a periodic channel; the (linearised) quasi-geostrophic, baroclinic flow shows a response on stochastic forcing which may serve as a parameterisation of the eddies. A wind driven ocean circulation is analysed numerically in a high resolution square basin employing the (nonlinear) shallow water system. Imposing spatially inhomogeneous random wind stress forcing generates a response with regime transitions which do not exist otherwise. From a more general perspective, a modular stochastic climate system emerges in the outlook.

CONTENTS

1. Climate and climate modelling	3
2. Zero-dimensional energy balance climate model	5
2.1. A two-stream radiative scheme	5
2.2. Statistic-dynamical climate model	6
2.3. Analysis: stability, sensitivity, and stochasticity	8
3. Quasi-geostrophic two-layer atmosphere in a channel	14
3.1. Quasi-geostrophy	15
3.2. Linear two-layer baroclinic model	17
3.3. Analysis: stability and stochasticity	19
4. Reduced gravity ocean in a square basin	27
4.1. Shallow-water equations and two-layer model	28
4.2. Reduced gravity model	29
4.3. Analysis of numerical experiments: Design, results, and interpretation	31
5. Summary and outlook	34
References	35

* From *Progress in Probability* (Birkhäuser Verlag, 2001) P. Imkeller and J.-S. von Storch (eds.)

1. Climate and climate modelling

The atmosphere cooperates with its companions in the climate system. These are the ocean, but also biosphere, pedosphere, cryosphere, and lithosphere play a prominent role. In each of these compartments the life-span of the largest energy containing perturbation characterises the predictability in terms of its decay period. Useful estimates of the memories and thus predictabilities of these sub-systems can be obtained from the different residence times of water as the most important carrier of latent energy. The observed large differences of the memories of the systems challenge monitoring and modelling of climate variability:

<i>compartments</i>	<i>time-scale estimates</i>
atmosphere	< 10 days (weather)
ocean/land	1 month (upper layers) to 10^3 years (deep ocean)
cryosphere	< 10 years (sea ice) to $> 10^3$ years (ice shields)

Climate modelling serves the *purpose* to improve understanding and forecasting in terms of relevant theoretical concepts and guidance for practically useful predictions; and most of the present models lie within these two extremes. Conceptual models require a small embedding dimension of the system's dynamics to be analysed while nonlinear prediction models incorporate almost all known effects. Consequently, experiments performed with these models fall into the categories of more or less sophisticated thought experiments or of highly elaborate numerical simulations:

<i>model</i>	<i>toy model</i>	<i>general circulation model</i>
purpose	conceptual understanding	practical forecast guidance
building	dimension as small as necessary	as large as possible
experiments	Gedanken experiment	simulation and prediction

Model building provides a suitable physical and spatial description of the climate system whose dynamics is based on fundamental conservation laws of thermal energy (first law of thermodynamics), momentum (Newton's law), and mass (continuity equation). Physical embedding can be achieved by a scale analysis leading to a spectrum of approximations describing geophysical fluid flow. It ranges from the shallow water equations and the quasi-geostrophic approximation (with the semi-geostrophic transform and hypo-geostrophy), via the primitive equations to the Boussinesq (and anelastic) system (see Pedlosky [23]). The primitive equations with the conservation of thermal energy and mass (air, salinity, water) provide the dynamical core of the present numerical weather prediction (NWP) and general circulation models (GCM). Spatially, the dynamics is decomposed in boxes, grids or layers, or spectral modes. Thus, as truncation is necessary, a parameterisation of the unresolved subgrid scale processes cannot be avoided.

Three equilibria characterise the geophysical fluid flow, two of which are related to the thermal energy and momentum equations: Hydrostatic and geostrophic

equilibrium characterise the dominating fluid forces in balance: vertical and horizontal pressure gradients and the accelerations induced by the earth's gravitation and rotation. The third equilibrium is related to radiative-convective processes. It describes the greenhouse representing an equilibrium between incoming short wave (solar) and outgoing long-wave (terrestrial) radiation including moist convective overturning. Deviations from these equilibria and their attractivity constitute the dynamics of the climate system.

The *experiments* with conceptual or low order systems differ from those conducted with climate or weather prediction models:

(i) Experiments with low order climate models are made to develop concepts and parameterisations of the underlying processes analysing stability, sensitivity, and the effect of stochastic forcing. *Stability analysis* refers to special trajectories like fix-points, limit cycles and their internal stability properties at fixed external parameters; furthermore, static and dynamic properties of attractors are deduced. The effect of changing external parameters shows routes to chaos based on changes of structural stability. In this sense, the variability of the climate system is understood through both its internal dynamics (El Nino-Southern Oscillation, biogeochemical interactions, nonlinearities) and the effect of external parameter changes (Milankovich cycles, changes of the solar radiation, volcanic activity, anthropogenic impacts). In practical applications related to the real climate system, *sensitivity analysis* provides insight into parameter changes modifying the equilibrium state of the global system (in a linear framework). The *stochastic analysis* is based on the two time scale approach, resolving the system's slow dynamics while parameterising the fast fluctuations by noise which, in turn, may generate resonant responses. Underlying this approach is the assumption of a spectral gap; it separates the slow system with large energy containing eddies from the fast low energy fluctuations, both of which follow different power law behaviour. Most relevant is the closure; here stochastic model parameters are adjusted to force the overall system to satisfy additional criteria, for example, the global entropy balance.

(ii) Experiments with comprehensive climate models have their origin in numerical weather predictions which, since the fifties and sixties, have been continuously improving; three day forecasts then had the quality of six day predictions now. Advances in model physics, data assimilation techniques, and computational power contributed to improve the forecast skill. Coupling of the atmosphere with the ocean, the sea ice, the continental ice shields, and the biosphere creates a hierarchy of GCMs to simulate the present and past climate as close to reality as possible analysing natural climate variability and the sensitivity on natural or anthropogenic impacts (for more details, see von Storch [29] in this volume).

Independent of their level of complexity, climate and weather models require the *parameterisation* of the fast and spatially unresolved processes. The time span which covers the dynamics to be parameterised depends on the time (and space) scales required for the *predictions of the first kind* (at fixed boundary conditions). The *predictions of the second kind* are made when a change of boundary conditions matters (see Table 1).

Table 1: Parameterisation and prediction of the first and second kind.

<i>lead time (days)</i>	<i>0.1</i>	<i>1</i>	<i>10</i>	<i>100</i>	<i>≥1,000</i>
atmosphere-ocean	parameterisation	<i>prediction of 1. kind</i>		prediction of 2. kind	

The outline of these lecture notes is as follows: Section 2 introduces the earth's greenhouse in terms of a zero-dimensional energy balance climate model; this minimal model serves as an example to demonstrate strategies of model building and analysis. A linear quasi-geostrophic atmosphere in a channel is described in section 3. Baroclinic instability, which is the origin of mid-latitude weather disturbances, is used to excite a response on stochastic forcing which resembles observed large scale atmospheric variability. Finally, section 4 presents a high resolution shallow water ocean in a square basin where the nonlinear response on idealised stochastic forcing due to atmospheric variability generates regime transitions.

2. Zero-dimensional energy balance climate model

To demonstrate climate modelling strategies, a minimum *energy balance* model is introduced first to provide the setting for the analysis of simple climate systems (for a review see Saltzman [26] and [28], North et al. [22]). It is based on a poor man's radiation scheme leading to the greenhouse climate system which, when in equilibrium, plays a similar role in climate dynamics as geostrophy and hydrostasy do in geophysical fluid flow. First, the dominant radiative fluxes contributing to the climate are defined in terms of a simple two-stream method, which is reduced to an atmosphere interacting with the land/ocean by radiative fluxes only; that is, sensible and latent heat fluxes are not explicitly considered. Parameterisation of the atmosphere by statistically deduced feedbacks leads to the statistic-dynamical model version, which is subjected to stability, sensitivity, and stochastic analysis in order to characterise climate variability.

2.1. A two-stream radiative scheme

A simple two-stream radiation scheme is confined to a single surface and two atmospheric layers which are associated with the respective heat capacities C (stratosphere, troposphere, and land/ocean with subscripts S, A, B). Long-wave (IR) or terrestrial radiative fluxes are described by the Stefan-Boltzmann law, σT^4 with $\sigma = 5.67 \cdot 10^{-8} \text{ W m}^{-2} \text{ K}^{-4}$. Note that, in the climate case, a linear law may suffice. The long-wave upward flux is partially absorbed in the next upper layer (absorption coefficients or emittance, α_A and α_S) and transmitted further (transmission coefficients $1-\alpha_A$ and $1-\alpha_S$). The long-wave downward radiation, however, is totally absorbed by the next lower layer. The short-wave (sw) or solar radiation, $I_o \sim 1360 \text{ W m}^{-2}$, passes a completely transparent atmosphere; it is absorbed at the bottom (land/ocean) from where a remaining part is reflected to space, $\frac{1}{4}I_o(1-a)$, with the (planetary) albedo or whiteness a (see, for example, Eliassen and Laursen

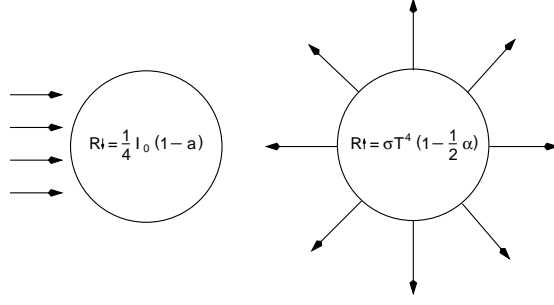


FIGURE 1. Incoming solar and outgoing terrestrial radiation of the zero-dimensional climate system.

[4]). Including absorption of solar radiation requires an additive term contributing to the radiative heating of the layer.

$$\begin{aligned}
 \text{stratosphere} \quad C_S(T_S)_t &= 0 + \alpha_S \alpha_B \sigma T_B^4 (1 - \alpha_A) + \alpha_S \alpha_A \sigma T_A^4 - 2\alpha_S \sigma T_S^4 \\
 \text{troposphere} \quad C_A(T_A)_t &= 0 + \alpha_A \alpha_B \sigma T_B^4 + \alpha_S \sigma T_S^4 - 2\alpha_A \sigma T_A^4 \\
 \text{land/ocean} \quad C_B(T_B)_t &= \frac{1}{4} I_o (1 - a) - \alpha_B \sigma T_B^4 + \alpha_A \sigma T_A^4
 \end{aligned}$$

At equilibrium (subscript 'o'), the incoming solar radiation, $R_o = \frac{1}{4} I_o (1-a)$, balances the terrestrial outgoing radiation: $R_o = R_{\downarrow} = R_{\uparrow}$.

2.2. Statistic-dynamical climate model

A minimum energy balance model is obtained discarding the stratosphere ($\alpha_S = 0$) but keeping the tropospheric emittance with $\alpha = \alpha_A \neq 0$. This yields the coupled greenhouse climate model with a black body land/ocean surface ($\alpha_B = 1$) and without solar absorption in the atmosphere (Fig. 1):

$$\begin{aligned}
 \text{atmosphere} \quad C_A(T_A)_t &= \{\sigma T_B^4 - 2\sigma T_A^4\} \alpha \\
 \text{land/ocean} \quad C_B(T_B)_t &= \frac{1}{4} I_o (1 - a) - \{\sigma T_B^4 - \alpha \sigma T_A^4\}
 \end{aligned} \tag{2.1}$$

Two approaches are commonly considered: (i) Modelling purely atmospheric variability, land and ocean remain fixed to provide the boundary conditions, $(T_B)_t = 0$. The dynamics is relatively fast due to the small heat capacity C_A .

$$\text{atmosphere} \quad C_A(T_A)_t = \left\{ \frac{1}{4} I_o (1 - a) - 2\sigma T_A^4 (1 - \frac{1}{2} \alpha) \right\} \alpha \tag{2.2}$$

where $C_A = c_p \frac{p_{sfc}}{g}$ with the surface pressure, $p_{sfc} \sim 1000 \text{ hPa}$, the specific heat, $c_p \sim 1005 \text{ J kg}^{-1} \text{ K}^{-1}$, and the Earth's acceleration, $g = 9.81 \text{ m s}^{-2}$. The incoming solar radiation, $\frac{1}{4} I_o (1 - a)$ with the planetary albedo, $a \sim 0.3$, and the emittance, $\alpha \sim 0.7$, lead to a stable equilibrium, $T_{Ao} \sim 240 \text{ K}$, to which all initial conditions, $T_A > 0$, converge. It corresponds to the observed temperature averaged over

the atmospheric mass, $\frac{p_{sfc}}{g} : T_{Ao} \sim \frac{1}{p_{sfc}} \int T_A dp$, which is close to that observed in the mid-troposphere near 500hPa. The linear stability, $(\delta T_A)_t = -\frac{1}{\tau_A} \delta T_A$, of the equilibrium solution, which defines the Newtonian cooling, is determined by the radiative time scale, $\tau_A = \frac{1}{4} C_A T_{Ao} (\alpha R_o)^{-1} \sim 1$ to 2 months.

(ii) Statistic-dynamical coupling of the fast atmosphere with a slow land and ocean requires a special strategy to model the dynamics of the slow system (T_B) and to make forecasts beyond the atmosphere's limit of predictability. A common approach is to parameterise the influence of the fast compartment (T_A). Here it leads to the *statistic-dynamical* climate model with feedbacks incorporating the statistical effects of the fast system. A similar strategy is employed for atmospheric global circulation models (AGCMs) when parameterising the fast and small scale processes of the boundary layer or cloud ensembles (after suitable space-time averaging).

Dynamical core (approximate inertial form): A suitable Ansatz for the parameterisation is a diagnostic atmosphere, $(T_A)_t = 0$. It reacts 'instantaneously' to changes of the slow system and feeds back to it by the Stefan-Boltzmann effect of the long-wave radiative fluxes of the atmosphere. This leads to the dynamical core of the statistic-dynamical model and its associated linear version:

$$\begin{aligned} \text{dynamical core} \quad C_B(T_B)_t &= \frac{1}{4} I_o (1-a) - \sigma T_B^4 (1 - \frac{1}{2} \alpha) \\ \text{linear version} \quad (\delta T_B)_t &= -\frac{1}{\tau_B} \delta T_B \end{aligned} \quad (2.3)$$

with the outgoing and incoming radiation, $\sigma T_B^4 (1 - \frac{1}{2} \alpha)$ and $\frac{1}{4} I_o (1-a)$. At equilibrium, the global surface temperature, $T_{Bo} = T_{Ao} \sqrt[4]{2} \sim 280 K$, exceeds the atmosphere's by about 20%. This characterises the *greenhouse effect* which corresponds to the vertical temperature gradient between surface and mid-troposphere: $T_{Bo} - T_{Ao} \sim 40 K$. Linearisation shows that the equilibrium is internally stable and all initial conditions $T_B > 0$ converge to it. The negative eigenvalue represents the inverse of the associated slow relaxation time scale, $\tau_B = \frac{1}{4} C_B T_{Bo} / R_o \sim 10$ to 20 months $\gg \tau_A$.

Parameterisations: The dynamical core of the system is completed by feedbacks which describe the effects of the fast variables on the slower ones. Linear feedbacks are most commonly used in climate modelling modifying the greenhouse climate by its albedo $a(T)$ and emittance $\alpha(T)$. Budyko [1] introduced the ice-albedo feedback as a linear regression. To simplify matters, the quadratic law, $a = a_2 - b_2 T^2$, will be adopted with fixed (empirical) coefficients a_2, b_2 . A positive albedo-feedback is obtained (satisfying $0 \leq a \leq 1$), which increases the albedo with temperature reduction:

a-feedback

temperature-albedo *temperature drop* \rightarrow *more snow* \rightarrow *higher albedo*
 albedo-temperature *less sw-radiation absorbed* \rightarrow *further temperature drop*

Swinbank [31] introduced a positive emittance-temperature feedback, $\alpha = \alpha(T_B)$,

from clear sky radiation measurements in the tropics, $\frac{1}{2}\alpha = c_2 + d_2 T_B^2$. While the CO_2 -effect can be associated with $c_2 = 0.235 \ln(CO_2)$ (CO_2 in ppm), the atmospheric moisture content modifies the emittance, $0 \leq \alpha \leq 1$, by a positive temperature feedback:

α -feedback

temperature-moisture *temperature-rise* \rightarrow *more evaporation* \rightarrow *more vapour*
 moisture-temperature *more IR radiation from sky* \rightarrow *further temperature rise*

Combination of the dynamical core with the (often empirically deduced) feedbacks defines the statistic-dynamical climate model whose external parameters are linked to natural and anthropogenic processes.

2.3. Analysis: stability, sensitivity, and stochasticity

Climate model analysis follows three paths: The *theoretical* approach of stability analysis applies nonlinear systems analysis methods. Here, catastrophes and resilience are the subjects of interest while other systems may show routes to chaos. More *practically* oriented is the estimate of climate sensitivity as the linear evolution near the stable equilibrium. Sensitivity analysis is often applied to data sets satisfying the global energy balance. Both analyses are basically deterministic and employed to identify and interpret stable fixpoints as climate means. They need to be complemented by the stochastic analysis to obtain estimates of higher moments. Here the Langevin approach, which is most commonly used in stochastic climate models, is adopted with white noise being added to the linearised system. Langevin or sensitivity approaches are similar in that the response of white noise or other impacts added to a linear system is analysed.

2.3.1. STABILITY ANALYSIS: The theoretical approach applies nonlinear systems analysis methods for which the predictions of the first and the second kind provide a suitable frame. The climate dynamics is described by a single variable gradient system, $T_t = f(T, p_i) = -dF(T, p_i)/dT$, associated with the potential F . It exhibits domains of structural changes or catastrophes and resilience depending on the external parameters p_i . A parameter μ (~ 1) is introduced to characterise changes of the intensity of the incoming solar radiation $\frac{1}{4}I_o$. Note that the subscript 'B' for the land/ocean temperature will be omitted in the following:

$$T_t = f(T, p_i) = \{d_2\sigma T^6 - (1 - c_2)\sigma T^4 + \mu\frac{1}{4}I_o b_2 T^2 + \mu\frac{1}{4}I_o(1 - a_2)\}C_B^{-1} \quad (2.4)$$

Prediction of the first kind describes the flow $T(t)$ commencing at $T(t_1)$, and its internal stability at fixed external parameters p_i ; *prediction of the second kind* characterises the effect of varying p_i associated with external or structural stability.

Internal stability at fixed external parameters is commonly analysed by perturbations δT on special trajectories like stable equilibria T_o , limit cycles, etc. Taylor expansion, $(T_o + \delta T)_t = f(T_o) + \frac{df}{dT}|_{T_o}(T - T_o) + \dots$, leads to the linear tangent version of the climate model, $\delta T_t = T_t - f(T_o) = J(T_o)\delta T$, whose eigenvalue is the inverse relaxation time scale, $\lambda = -\frac{df}{dT}|_{T_o} = -\frac{1}{\tau_B}$. As $f = -\frac{dF}{dT}$ is the

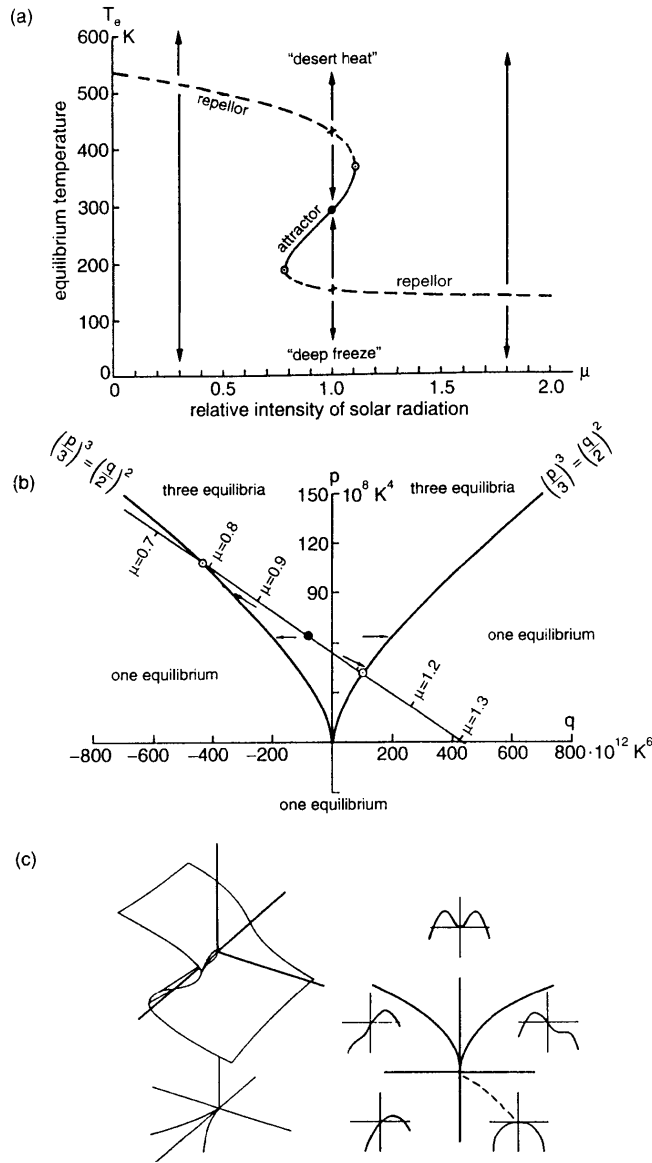


FIGURE 2. Zero-dimensional climate system with combined ice albedo and greenhouse feedback: a) Equilibria on a cross-section through state space, b) bifurcation diagram on a parameter plane of the generalised polynomial of (2.4), and c) schematic presentation of the potential of a gradient system (see Fraedrich [6]).

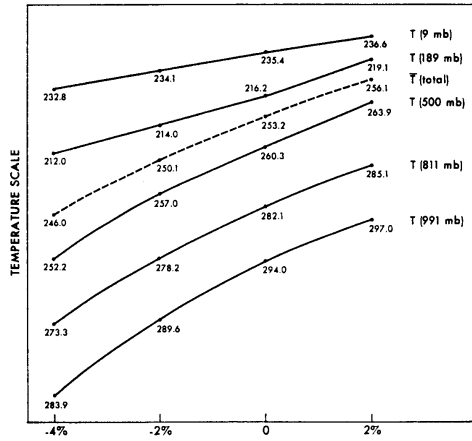


FIGURE 3. GCM-experiment (after Weatherald and Manabe [33]): Area-mean temperatures (in K) at various levels (indicated on the right margin) versus changing incoming solar radiation (in percent).

gradient of a potential $F(T, p_i)$, the equilibrium solution T_o corresponds to an extremum or saddle-point in the cross-section of the state-parameter or (T, p_i) -space where $f(T_o) = -\frac{dF}{dT} = 0$. Its internal instability is defined by an F-maximum which depends on the sign of the eigenvalue, $\lambda = \frac{d^2F}{dT^2}|_{T_o} < 0$.

External stability is associated with the prediction of second kind and the system's sensitivity to changing external parameters or boundary conditions. This can be characterised qualitatively by catastrophes in the state-parameter or (T_o, p_i) -space by $J(T_o) = \frac{df}{dT}|_{T_o} = \frac{d^2F}{dT^2}|_{T_o} = 0$: Bifurcation occurs where a stable and an unstable fix-point coincide leading to a fold-catastrophe at T_o^* ; the coalescence of two folds defines a cusp, T_o^{**} :

$$\begin{aligned}
 \text{fold} \quad & f(T_o^*, p_i) = 0, & \frac{df}{dT}|_{T_o^*} &= 0 \\
 \text{cusp} \quad & f(T_o^{**}, p_i) = 0, & \frac{df}{dT}|_{T_o^{**}} &= 0, & \frac{d^2f}{dT^2}|_{T_o^{**}} &= 0
 \end{aligned} \tag{2.5}$$

The results are summarised in Fig. 2. There is a stable equilibrium, T_o , representing today's greenhouse climate. The two neighbouring fix points at the same external parameter constellation are unstable and act as repellers defined by the maxima of the potential $F(T)$. All initial conditions in their environment are attracted by the stable equilibrium T_o , or the 'deep freeze' and 'boiling heat' bounds limited by $\alpha = (0,1)$ or $\alpha = (0,1)$. The direction of the flow depends on the sign induced by the incoming and outgoing radiation difference, $R_{\downarrow} - R_{\uparrow}$. Changing external parameters reveals the generic configuration of two fold-catastrophes with stable and unstable equilibria coalescing. One of these catastrophes is attained,

for example, when reducing the incoming solar radiation or the parameter μ . Note that GCMs (Manabe and Weatherald [33], Fig. 3) revealed similar behaviour when reducing solar radiation with ice conditions approaching.

More variables complicate matters but add interesting dynamical features (Saltzman et al. [27], Källén et al. [16]). For example, the ice-albedo feedback can be extended introducing the latitudinal extent of the sea-ice or the continental ice-sheet, respectively, as a new state variable, which interacts with the global energy balance. The sea-ice extent acts as an insulator for the global temperature represented by the ocean. The dynamics of the continental ice-shield is linked to the global temperature through the ice-albedo feedback; here the position of the snow-line separating accumulation and ablation zones needs to be parameterised by the global temperature.

2.3.2. SENSITIVITY ANALYSIS: The sensitivity analysis is a more practical approach to determine the system's linear behaviour near its stable equilibrium. Before evaluating climate variance formally by the stochastic analysis (see below), the effect of changing feedback parameters on climate, assuming these to be part of the dynamical system, is estimated. It is commonly applied to global data sets satisfying the global energy balance at equilibrium (see textbooks, Hartmann [11]). Near the stable T_o -equilibrium the linear response of the system to small variations of external parameters defines the sensitivity in terms of global mean surface temperature variations δT_o :

$$\begin{aligned} \text{climate sensitivity} & \quad \tau_B(\delta T)_t = -\delta T + \{\text{sensitivity}\} & (2.6) \\ \text{sensitivity (in K)} & \quad \delta T_o = \frac{1}{4}T_o\{\delta_a + \delta_\alpha\} \end{aligned}$$

where the co-albedo and co-emittance variations are $\delta_a = -\delta a/(1-a)$ and $\delta_\alpha = \frac{1}{2}\delta\alpha/(1-\frac{1}{2}\alpha)$. Setting $(\delta T)_t = 0$, relates small external parameter variations to changes of the equilibrium temperature leading to the sensitivity $\beta = \frac{1}{4}T_o(\delta_a + \delta_\alpha)$, which is commonly applied to various external parameters r : $\beta(r) = \delta T_o(r) = rT_r$. That is, a $\beta(r) = 0.01\delta T_o$ shift of the equilibrium temperature is caused by a 1% change in the parameter, r , keeping all others constant. Two sensitivities are of particular interest because of their association with global change issues of anthropogenic and natural impact on the climate system. They are related to changes of the CO_2 -concentration in ppm, $c_2 = 0.235 \ln(CO_2)$, and to changes of the incoming solar radiation μ associated with astronomical cycles. Polar and tropical regions may be distinguished by the dominance of the ice-albedo and the moisture-emittance feedback, respectively. Thus, changing the incoming solar radiation by 1% (the ice-age reduction is about 1.6%) shows that the polar sensitivity is twice as large as the tropical response with 1.9K versus 0.9K. Note that the Stefan-Boltzmann effect (designated as 'no-feedback') gives about 0.7K (see Table 2). A similar result is obtained for CO_2 -doubling (a 100% change): The polar response

Table 2: Sensitivity of the greenhouse climate due to changes of solar radiation, $\beta(\mu)$, and carbon dioxide, $\beta(CO_2)$.

feedback	sensitivity (in K)	
	$\beta(\mu)$	$\beta(CO_2)$
no	72	1.7
albedo (polar)	191	4.5
emittance (tropical)	90	3.0
albedo and emittance	413	13.7

exceeds the tropical by 30% with a 4.5K sensitivity compared to 3.0K. Introducing the moisture-emittance feedback almost doubles the CO_2 -sensitivity of the no-feedback climate from 1.7 to 3.0K.

Two comments are in order: (i) For a complete sensitivity analysis the dependence of the single external parameter r on all other parameters p_i needs to be included, $\frac{dT}{dr} = \frac{\partial T}{\partial r} + \sum_i \frac{\partial T}{\partial p_i} \frac{\partial p_i}{\partial r}$. Here, however, these relations are discarded assuming all other factors being constant. (ii) A positive feedback destabilises the system only, if a perturbation grows, which implies positive eigenvalues of the linearised system. At fixed external parameters the variations of albedo and emittance are $\delta a = -2b_2 T_o \delta T$ and $\frac{1}{2} \delta \alpha = 2d_2 T_o \delta T$. Therefore, the two linear regression-type positive feedbacks ($b_1 = 2b_2 T_o$, $d_1 = 2d_2 T_o$) do not alter the system's internal stability, if $0 < b_1 < 4(1 - a_o)/T_o \sim 0.01$ and $0 < d_1 < 4(1 - \frac{1}{2}\alpha_o)/T_o \sim 0.01$.

2.3.3. STOCHASTIC ANALYSIS: The deterministic sensitivity analysis provides information about climate variability by feedback induced changes of albedo or emittance. It is complemented by a stochastic analysis of the linear tangent model to obtain explicit estimates of the climate variance. This leads to the Langevin climate with white noise being added to the linearised system (replacing the feedback sensitivities). The distinctly different time scales involved, $\tau_B \gg \tau_A$, may be visualised as an analogue of the Brownian motion with its small and fast moving particles exciting the large and slowly hovering ones (Hasselmann [12]). In this sense the white noise is a parameterisation of the fast atmosphere's fluctuations (τ_A) forcing the linearised slow climate system (τ_B) to a response which characterises climate variability:

$$\begin{aligned} \text{Langevin's climate} \quad \delta T_t &= -\frac{1}{\tau_B} \delta T + \{\text{noise } \epsilon_A(t)\} \\ \text{noise variance} \quad \sigma_A^2 &= \frac{1}{\tau_A} q \end{aligned} \quad (2.7)$$

Stochastic forcing acts as a white noise energy injection rate parameterising the sensible and latent heat exchanges. Formally, the auto-covariance describes the infinitesimally short memory of the delta-correlated fluctuations acting on the climate system: $\langle \epsilon_A(t) \epsilon_A(t+s) \rangle = q \delta(s) \sim \frac{1}{\tau_A} q \sim \sigma_A^2 \exp(-\frac{1}{\tau_A} |s|)$ with the white noise spectrum or forcing intensity q .

Closure by entropy balance: Stochastic forcing and the dynamic response of the climate system are limited by global energy and entropy constraints that are satisfied by both the fast and the slow system. This leads to a closure which, in general, arises when coupling the fast parameterised with the slow resolved dynamics. A first order closure links the stochastic forcing intensity with the large scale asymptotic response realizing the global entropy balance of the atmosphere as the gas working for the greenhouse heat engine. At equilibrium, its efficiency η is a measure of the portion, $\eta R_o = D$, of the incoming solar radiation, which is converted into mechanical energy (or dissipation D). It drives the atmospheric motion by convective overturning exchanging airmasses between surface (T) and aloft (T_A). These motions force the variability of the slow climate system by stochastically fluctuating energy injections; they are measured in terms of temperature changes (divided by the land/ocean heat capacity C) and the slow relaxation time scale τ_B :

$$\text{closure} \quad \sigma_A = \frac{D}{C_B} = \eta \frac{R_o}{C_B} = \frac{1}{4} \eta \frac{T_o}{\tau_B} \quad \text{and} \quad \sigma_A^2 = \frac{q}{\tau_A} \quad (2.8)$$

As the working fluid is the atmosphere, and the greenhouse is the heat engine, the global climate system does not deliver the mechanical energy to space but keeps it through dissipation. Thus the mechanical energy dissipation D at temperature, T_D , contributes to the entropy budget and remains part of the global energy balance instead of being extracted. In this sense Margules' approach on the energetics ('Über die Energie der Stürme' [20]) is extended here by the appropriate entropy balance. In equilibrium this leads to an efficiency of the atmosphere contrasting Carnot's reversible case which is related to technical heat engines:

	<i>Margules</i>	<i>Carnot</i>	
energy	$0 = R\downarrow - R\uparrow$	$0 = R\downarrow - R\uparrow - D$	(2.9)
entropy	$0 = S\downarrow - S\uparrow + S_{int}$	$0 = S\downarrow - S\uparrow$	
efficiency	$\eta = \eta_{rev} T_D / T_{Ao}$	$\eta_{rev} = 1 - T_{Ao} / T_o$	

Import, export, and internal generation of entropy are $S\downarrow = R\downarrow / T_o$ and $S\uparrow = R\uparrow / T_{Ao}$, and $S_{int} = D / T_D$. The efficiency of the greenhouse, $\eta = D / R\downarrow \sim 16\%$, depends on the temperature, $T_D \sim \frac{1}{2}(T_{Ao} + T_o)$, attributed to the internal entropy generation and the Carnot efficiency, $\eta_{rev} \sim 1 - \sqrt[4]{2} \sim 15\%$. Note that in Carnot's reversible case, the entropy import balances the export and the mechanical energy D is extracted from the system's energy balance, where it remains in Margules' case.

Climate response: The stochastic differential equation can be solved by standard methods (see, for example, Gardiner [10]). Given the white noise forcing variance, $\sigma_A^2 = (\eta R_o / C_B)^2 = q / \tau_A$, and the decorrelation time scales of the fast and the slow systems, τ_A and τ_B , the asymptotic response can be quantified by the variance spectrum, $S(\omega)$, employing the Fourier transform (Fig. 4), or denoting the total variance, $\sigma^2 = q \tau_B = \sigma_A^2 \tau_A \tau_B$:

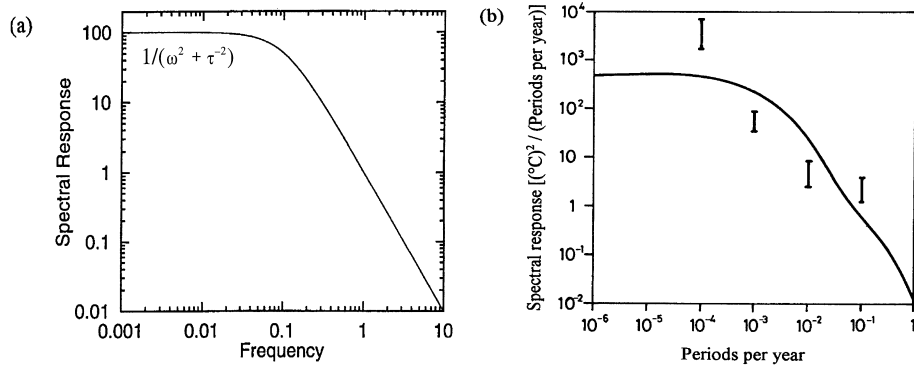


FIGURE 4. Spectral response of the Langevin climate system on white noise stochastic forcing: (a) theoretical and (b) observed (after Kutzbach and Bryson [17], and Lemke [18]).

response spectrum

$$S(\omega) = q/(\omega^2 + \tau_B^{-2}) \quad (2.10)$$

standard deviation (in K)

$$\sigma = \frac{1}{4}\eta T_o \sqrt{\frac{\tau_A}{\tau_B}}$$

The response spectrum, $S(\omega)$, of the stochastically forced Langevin climate is characterised by the following regimes in the frequency domain (Fig. 4): For high frequencies ($\omega > \frac{1}{\tau_B}$) the stationary spectral response attains a red noise power law, $S \sim \omega^{-2}$, with variance densities rising from high to low frequencies. In the low frequency domain ($\omega < \frac{1}{\tau_B}$) a flat white spectral plateau emerges with $S \sim q\tau_B^2$ (Fig. 4). Given an order of magnitude difference between time scales of the fast and slow components of the climate system, $\frac{\tau_A}{\tau_B} \sim 0.1$, the efficiency of the greenhouse heat engine, $\eta \sim 16\%$, and the stable equilibrium, $T_o \sim 280 K$, we obtain a stochastic response measured by the temperature standard deviation, $\sigma = \sqrt{\langle \delta T^2 \rangle} \sim 3 K$, of the climate system. Both red noise spectrum and response intensity are in qualitative agreement with the observed climate variability.

3. Quasi-geostrophic two-layer atmosphere in a channel

Highs and lows are synoptic scale eddies with remarkable influence on the climate, its variability in the mid-latitudes and in the tropics. Therefore, climate modelling cannot be pursued without incorporating these weather processes in parameterised format or explicitly resolving them. A minimum linear dynamical system of the quasi-geostrophic flow in a zonal channel is introduced as a 'toy weather model' to illustrate some dynamical and energetical aspects of the weather systems related to the classical baroclinic instability problem. Responses to damping and to stochastic forcing conclude the analysis. They are attributed to the larger and the smaller

scales (Fig. 5), which embed the midlatitude synoptic disturbances. This leads to realistic estimates of the space-time variability representing mid-latitude storm tracks which, ultimately, may serve as the stochastic input to the ocean model (section 4). First, the basic approximations underlying quasi-geostrophy are briefly summarised (for more details see Holton [13], Pedlosky [23]).

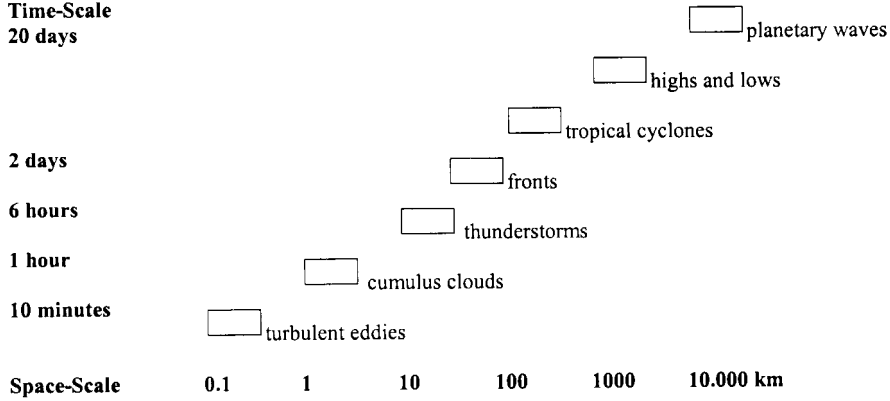


FIGURE 5. Space-time scales of atmospheric phenomena.

3.1. Quasi-geostrophy

The quasi-geostrophic flow is the basis for toy models describing mid-latitude synoptic systems (Fig. 5). General assumptions are a shallow atmosphere, whose vertical extent is small compared to the earth's radius, so that hydrostasy can be employed balancing gravity and the vertical pressure gradient force:

$$\text{hydrostasy} \quad 0 = -\rho^{-1}p_z - g \quad (3.1)$$

Thus pressure p can be used as the vertical coordinate and its height z (or geopotential gz) as an independent variable. The density ρ satisfies the equation of state, $p = \rho RT$, with the gas constant R so that the temperature can be expressed in terms of thickness, $T = -pR^{-1}gz_p$. The balance of Coriolis and horizontal pressure gradient forces defines the geostrophic wind, $f_o \mathbf{u}_g = f_o(u_g, v_g) = g(-z_y, z_x)$, with the Coriolis parameter, $f_o = 2\Omega \sin(\text{lat}) \sim 1.12 \cdot 10^{-4} \text{s}^{-1}$, at latitude $\text{lat}=50^\circ$ and the Earth's rotation rate, $\Omega \sim 2\pi \text{day}^{-1}$. Variation of the Coriolis parameter is often introduced by a β -plane approximation, $f = f_o + \beta y$ where $\beta = f_y = 2\Omega a^{-1} \cos(\text{lat}) \sim 1.471 \cdot 10^{-11} \text{m}^{-1}$. On constant pressure levels the geostrophic flow follows the geostrophic streamfunction, $\psi = \frac{1}{f_o}gz$, which does not contribute to the mass balance

$$\text{continuity} \quad u_x + v_y = -\omega_p \quad (3.2)$$

so that the vertical mass flux, $dp/dt = \omega \sim -\rho g w$ with $w = dz/dt$, is determined by the ageostrophic part of the windfield, $\mathbf{u}_a = \mathbf{u} - \mathbf{u}_g$.

Quasi-geostrophy may now be introduced as an approximate inertial form (in a similar manner as the dynamical core of the statistic-dynamical climate system) assuming the adjustment to geostrophy to occur instantaneously. This can be parameterised as a diagnostic process effecting the change of horizontal momentum, $d\mathbf{u}/dt \sim d_g \mathbf{u}_g/dt$. It feeds back to the dynamics through the ageostrophy induced vertical mass flux due to the imbalance between Coriolis and pressure gradient forces effecting the momentum and the thermal energy equations:

$$\begin{aligned} \text{zonal momentum} & \quad \left(\frac{\partial}{\partial t} + \mathbf{u}_g \cdot \nabla\right) u_g = +f v - g z_x & (3.3) \\ \text{meridional momentum} & \quad \left(\frac{\partial}{\partial t} + \mathbf{u}_g \cdot \nabla\right) v_g = -f u - g z_y \\ \text{thermal energy} & \quad \left(\frac{\partial}{\partial t} + \mathbf{u}_g \cdot \nabla\right) T = \omega S \end{aligned}$$

Damping, F_x, F_y , and diabatic warming, Q/c_p , may be added to the rhs. The ωS -term comprises both the vertical temperature advection, ωT_p , and the pressure work, $\rho dp/dt$. The static stability, $S = \sigma \frac{p}{R} = -T_p + \frac{R}{c_p} \frac{T}{p}$, is assumed to remain unchanged. For further analysis this system is conveniently reduced to equations of vorticity, $\zeta_g = \nabla^2 \psi$, and thermal energy:

$$\begin{aligned} \text{vorticity} & \quad \left(\frac{\partial}{\partial t} + \mathbf{u}_g \cdot \nabla\right) \nabla^2 \psi + \beta \psi_x = f_o \omega_p & (3.4) \\ \text{thermal energy} & \quad \left(\frac{\partial}{\partial t} + \mathbf{u}_g \cdot \nabla\right) \psi_p = -\frac{\sigma}{f_o} \omega \end{aligned}$$

Eliminating ω shows that the quasi-geostrophic potential vorticity, $W = f_o + \beta y + \nabla^2 \psi + (f_o^2/\sigma) \psi_{pp}$, is conserved for adiabatic quasi-geostrophic flow. Combination provides the diagnostic ω -equation describing the secondary circulation of the flow:

$$\omega\text{-equation} \quad \nabla^2 \omega + \frac{f_o^2}{\sigma} \omega_{pp} = \frac{f_o}{\sigma} \{ \mathbf{u}_g \cdot \nabla (\nabla^2 \psi + f) \}_p - \frac{f_o}{\sigma} \nabla^2 (\mathbf{u}_g \cdot \nabla \psi_p)$$

Upward motion is caused by differential vorticity advection (of upper cyclone, near surface anticyclone) or warm air advection (by upper high, near surface low). This secondary circulation is induced by the imbalance between Coriolis and pressure gradient forces so that the height adjusts to the vorticity field (rhs first term) and vice versa (rhs second term).

A more formal derivation of the quasi-geostrophic system is based on the estimate of $|\mathbf{u}_a|/|\mathbf{u}_g| \sim O(Ro) \ll 1$ by the Rossby number, inertial/Coriolis force or $Ro = \frac{U}{f_o L}$, whose smallness is a measure of the validity of geostrophy (for details of a perturbation theory in terms of the Rossby number see Pedlosky [23]). In summarising quasi-geostrophy, we follow Holton [13]: The momentum (and its rate of change following the horizontal flow) can be approximated by its geostrophic

value (and its rate of change following the geostrophic wind) and the small vertical advection can be neglected. As the vorticity is constrained to be geostrophic, the vertical motion, which is uniquely determined by the geopotential height field, ensures that vorticity changes will be geostrophic.

3.2. Linear two-layer baroclinic model

A minimum model describes the quasi-geostrophic flow in a linear two-level, f-plane channel spanned by (x, y, p) -coordinates. The dynamics is reduced to upper and lower layer vorticity equations (Fig. 6). They are formulated on two pressure levels (subscripts 1 and 3), $p_1 = 250$ and $p_3 = 750 hPa$ of $\Delta p = 500 hPa$ difference, and coupled by the thermal energy equation at the 500hPa level (subscript 2). Top and bottom levels (subscript 0 and 4) satisfy the boundary conditions associated with the vorticity at the levels 1 and 3 without or with massflux injection. That is, a vertical massflux induced by boundary layer friction (Ekman pumping).

Levels		Variable	Equation
0mb	0-----	$\omega_0 = 0$	or $\neq 0$: Ekman pumping
250mb	1.-.-.-.	ψ_1	Vorticity
500mb	2-----	ω_2	Thermal Energy
750mb	3.-.-.-.	ψ_3	Vorticity
1000mb	4-----	$\omega_4 = 0$	or $\neq 0$: Ekman pumping

FIGURE 6. Vertical structure of the two-layer baroclinic model.

Linearisation leads to perturbations, $u'_{1,3} = u_{1,3} - U_{1,3}$ etc., about the basic state with upper and lower layer zonal current, $U_{1,3}$, which is separated into the barotropic and baroclinic contributions: the vertical mean, $U = \frac{1}{2}(U_1 + U_3) \sim 10 \text{ ms}^{-1}$, and the difference or half-shear, $U_T = \frac{1}{2}(U_1 - U_3) \sim 10 \text{ ms}^{-1}$. The thermal wind, $2U_T$, is a measure of the baroclinicity. Due to geostrophy of the basic state, the thermal wind is related to the meridional temperature gradient, $T_y = \Delta_y T / L_y$, and characterises the mid-latitudes with mixing of the warm subtropical and cold polar air, $\Delta_y T \sim 25 \text{ K}$:

$$\begin{aligned} \text{thermal wind} & \quad 2U_T = -\frac{R}{f_o} T_y \ln\left(\frac{p_3}{p_1}\right) \sim 20 \text{ ms}^{-1} \\ \text{static stability} & \quad \sigma = +\frac{R}{p} S \sim 3 \cdot 10^{-6} \text{ m}^2 \text{ Pa}^{-2} \text{ s}^{-2} \end{aligned}$$

The static stability realizes the radiative greenhouse effect with the mean temperature, $T_2 \sim T_{Ao}$ at 500 hPa, and the vertical gradient, $T_p = \Delta_p T / \Delta p$ with $\Delta_p T = T_3 - T_1 \sim 50 \text{ K}$. It enters the Rossby radius of deformation, $\kappa^{-1} = \frac{\Delta p}{f_o} \sqrt{\sigma} \sim 720 \text{ km}$ (or $\kappa \sim 6k_1$ or wavenumber six), which describes the horizontal distance travelled

by an internal gravity wave during a pendulum day. The zonal extent of the periodic channel, $L_x = 2\pi a \cos(50^\circ) \sim 25000 \text{ km}$, corresponds to the fundamental zonal wavenumber one, $k_1 = 2\pi/L_x$. Meridionally, the channel extends over a 30° belt about 50° latitude, which defines a fundamental half-wavelength, $L_y = 3400 \text{ km}$, or meridional wavenumber, $l_1 = \pi/L_y$. These values remain unchanged in the subsequent stability analysis. Finally, perturbations of the geostrophic streamfunction are separated into an external barotropic, $\psi = \frac{1}{2}(\psi_1 + \psi_3)$, and a baroclinic or first internal mode, $\theta = \frac{1}{2}(\psi_1 - \psi_3)$; $\nabla^2(\psi, \theta)$ and $(\psi, \theta)_x$ represent the respective vorticities and the meridional geostrophic wind components. The β -term may be included by adding the planetary vorticity advection, $\beta\psi_x$ or $\beta\theta_x$, to the baroclinic or barotropic equations:

$$\begin{aligned} \text{barotropic} \quad & \left(\frac{\partial}{\partial t} + U\frac{\partial}{\partial x}\right)\nabla^2\psi + U_T(\nabla^2\theta)_x = F_\psi \quad (3.5a) \\ \text{baroclinic} \quad & \left(\frac{\partial}{\partial t} + U\frac{\partial}{\partial x}\right)(\nabla^2\theta - 2\kappa^2\theta) + U_T(\nabla^2\psi + 2\kappa^2\psi)_x = F_\theta \end{aligned}$$

Parameterisations: To analyse variability induced by stochastic forcing (z), damping is required to ascertain asymptotic equilibrium and prevent the system from instability:

$$\text{forcing} \quad F_\psi = -\frac{1}{2}f_o(\omega_o - \omega_4)/\Delta p + z_\psi(t) \quad F_\theta = -\frac{1}{2}f_o(\omega_o + \omega_4)/\Delta p + z_\theta(t)$$

Ekman pumping, $\frac{f_o}{\Delta p}\omega_{o,4} = -r_{1,3}\nabla^2\psi_{1,3}$, is associated with relaxation time scales, $r_{1,3} \sim 1.25 \text{ day}^{-1}$, denoted as Rayleigh damping. The simplest form is upper and lower lid pumping of the same intensity, $r = r_1 = r_3$, which may be interpreted by friction at the lower boundary and, at the upper boundary, by export into the barotropic component U of the basic state, where it dissipates at the same rate:

$$-\frac{1}{2}f_o(\omega_o - \omega_4)/\Delta p = -r\nabla^2\psi \quad -\frac{1}{2}f_o(\omega_o + \omega_4)/\Delta p = -r\nabla^2\theta$$

Stochastic forcing is introduced as a white noise vorticity injection rate (DelSole and Farrell [3], and not as a momentum injection). It is parameterised by vertical mass fluxes through the upper and lower lid and adds to the deterministic contribution of Ekman-pumping. Associated with these vertical mass fluxes, we assume that vertical overturning provides the stochastic input: warm and cold fronts, convective complexes, up- or downdrafts at the top of the boundary layer and anomalous energy import or export from an overcast or cloud-free top level (in terms of deviations from the basic state):

$$z_\psi = \sum_{k,l} \epsilon_{\psi,kl}(t) \sin(ly) \exp(ikx) \quad z_\theta = \sum_{k,l} \epsilon_{\theta,kl}(t) \sin(ly) \exp(ikx)$$

Without stochastic forcing, the meridional temperature difference drives the atmospheric motion by baroclinic instability. This flow exchanges airmasses through slantwise convection from the subtropical lower-layers to the sub-polar upper layers (and vice versa) and decays due to Ekman-pumping which represents lower layer friction and upper layer export to the larger planetary or the zonal mean

basic state U . The cycle may be closed by the baroclinically induced meridional eddy heat flux divergence; it can be used to feed the baroclinic part of the basic state flow U_T , and thus change the thermal wind. The subsequent reduction of the meridional temperature gradient is adjusted by radiative processes by Newtonian cooling. Thus, at equilibrium, the eddy kinetic energy generation is balanced by damping or dissipation while the excitation by stochastic forcing generates the system's variability.

Spectral model: The separation $\{\psi, \theta\} = \{\Psi_{kl}(t), \Theta_{kl}(t)\} \sin(l y) \exp(ikx)$ transforms the (ψ, θ) -perturbations from the (x, y) -space to the zonal and meridional wavenumber or (k, l) -domain by a superposition of orthogonal eigenfunctions. The transformation replaces the partial differential equations by a spectral model in terms of a set of autonomous ordinary differential equations describing the time-evolution of the complex amplitudes, $(\Psi_{kl}, \Theta_{kl}) = (\Psi_{kl}, \Theta_{kl})_r + i(\Psi_{kl}, \Theta_{kl})_i$; the subscripts k, l will be omitted in the following:

$$\begin{aligned} \text{barotropic} \quad K^2 \Psi_t &= -ikK^2 U \Psi - ikK^2 U_T \Theta - rK^2 \Psi + \epsilon_\psi & (3.5b) \\ \text{baroclinic} \quad (K^2 + 2\kappa^2) \Theta_t &= -ikU_T (K^2 - 2\kappa^2) \Psi - ikU (K^2 + 2\kappa^2) \Theta - rK^2 \Theta + \epsilon_\theta \end{aligned}$$

with the total wavenumber, $K^2 = k^2 + l^2$, and the stochastic vorticity injection rate $(\epsilon_\psi, \epsilon_\theta)$.

3.3. Analysis: stability and stochasticity

The model analysis follows two tracks: Baroclinic instability describes the asymptotic growth and decay of the system with and without damping; the phase relation and the energy cycle offer further insight to the physical processes. The stochastic analysis leads to a quantitative measure of space-time variability. Again, the Langevin approach is adopted with white noise being added to the linearised system. The frequency-wavenumber spectra of the geopotential height (or meridional geostrophic wind) and the eddy meridional heat flux are deduced. Coupling with the overall entropy budget provides a first order closure to derive the magnitudes of stochastic forcing and its response.

3.3.1. BAROCLINIC INSTABILITY ($r = 0, \epsilon = 0$): Cast in matrix form the spectral model (3.5) gives $\mathbf{L}\Phi_t = \mathbf{J}\Phi$ with $\Phi = (\Psi, \Theta)^T$. Linear stability analysis reduces to the eigenvalue-problem of the linear operator \mathbf{J} , $\mathbf{J} + i\omega\mathbf{L} = 0$, replacing the time derivative by $-i\omega$. Eigenvalues $'\omega'$ (denoting angular frequencies) and eigenvectors characterise the *asymptotic* ($t \rightarrow \infty$) or normal mode behaviour of the solution. The real part of the complex eigenvalues ω leads to the zonal phase speed, $Re(\omega) = ck$, and the growth or decay rates are defined by the imaginary part, $Im(\omega) = \omega_i > 0$ or < 0 :

$$\begin{aligned} \text{dispersion(no damping)} \quad \det(\mathbf{J} + i\omega\mathbf{L}) &= 0 & (3.6) \\ \text{asymptotic frequency} \quad \omega - Uk &= \pm iXU_T k \end{aligned}$$

with $X^2 = \frac{2\kappa^2 - K^2}{2\kappa^2 + K^2}$. The real and imaginary parts of the eigenfrequencies are presented in a frequency-wavenumber or (ω, k) -diagram (Fig. 7a) which shows the basic features of baroclinic instability as discussed by Eady in his seminal 1949-paper [5]:

(i) *Short* wave perturbations, $K > \sqrt{2}\kappa$ are neutral ($\omega_i = 0$), and propagate with two different zonal phase speeds which, for small waves, $K \rightarrow \infty$, tend towards the basic zonal flow of the upper and lower layer, $c = U \pm U_T$. That is, both layers are uncoupled (Fig. 7a, curved lines).

(ii) *Long* wave perturbations $K < \sqrt{2}\kappa$ are unstable ($\omega_i > 0$), couple upper and lower layer and, therefore, propagate with the vertically averaged zonal flow, $c = Re(\omega)/k = U$ (Fig. 7a, straight line). The coupling commences at the bifurcation point $(K_b)^2 = 2\kappa^2$; maximum growth occurs at $K_{max}^2 = 2\kappa\sqrt{\kappa^2 - k^2}$ or $k_{max}^2 = -(2\kappa^2 + l^2) \pm 2\kappa\sqrt{(2\kappa^2 + l^2)}$ which, for $l = 0$, reduces to $2\kappa^2(\sqrt{2} - 1)$.

(iii) *Phase* structures of the baroclinically unstable waves (Fig. 8 top panel) demonstrate further properties associated with the barotropic and baroclinic modes. Being perpendicular, their wave solutions are shifted by $\frac{1}{2}\pi$, which specifies the separation Ansatz

$$\begin{aligned}\psi &= \Psi_o \exp(\omega_i t) \sin(ly) \sin\{k(x - Ut)\} \\ \theta &= \Theta_o \exp(\omega_i t) \sin(ly) \cos\{k(x - Ut)\}\end{aligned}$$

Substitution into the spectral model provides the amplitude and phase relations independent of the mean zonal steering flow U . Discarding the Doppler shift by setting $U = 0$ does not change the results: $\Theta_o = \Psi_o \omega_i (kU_T)^{-1} = \Psi_o X$ with $\tan(\alpha) = X$. Now the slope of the trough axis of the unstable waves can be determined. It is tilted westward by a phase shift of $2\alpha \leq \frac{1}{2}\pi$ from the lower to the upper layer height field (or $\alpha \leq \frac{1}{4}\pi$ to the mid-level temperature or θ -field, Fig. 8):

$$\psi_{1,3} = \psi \pm \theta = \Psi_o \exp(\omega_i t) \sin(ly) \sin\{k(x - Ut) \pm \alpha\} / \cos(\alpha)$$

which, for maximum growth, is about 65° . Similarly, the mid-level temperature wave and the vertical motion (secondary circulation) are derived using the thermal energy equation with zonal, meridional, and vertical temperature advection by the mean and eddy flow:

$$\text{thermal energy} \quad \theta_t + U\theta_x - \psi_x U_T = \frac{1}{2} \frac{\sigma \Delta p}{f_o} \omega_2$$

The ω_2 -wave, $\omega_2 = \Omega_o \exp(\omega_i t) \sin(ly) \cos\{k(x - Ut)\}$ with $\Omega_o = 2(\omega_i \Theta_o - U_T k \Psi_o) \frac{f_o}{\sigma \Delta p}$, is in phase with the θ -wave and reveals sinking cold and rising warm air masses. This constitutes a secondary circulation extracting kinetic perturbation energy $\omega_2 \theta$ through eddy available potential energy by the meridional eddy heat flux $\Psi_x \theta$ (see perturbation energetics and Lorenz energy cycle). Further physical processes are related to the vorticity changes in both layers. They are induced by zonal advection and stretching:

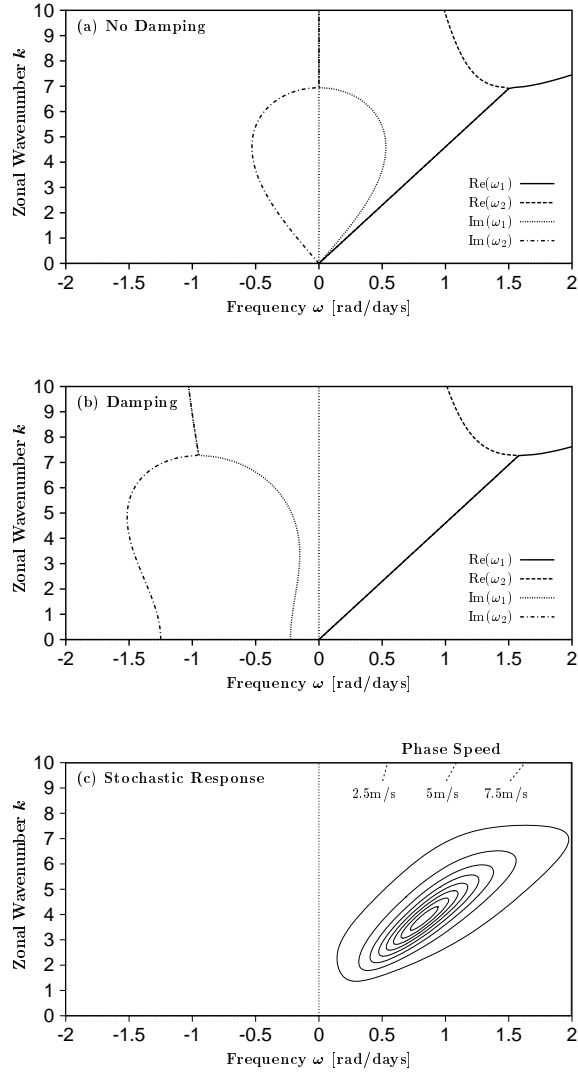


FIGURE 7. Frequency-wavenumber diagram (along 50° latitude) for the f-plane two-layer baroclinic model: Real and imaginary parts of eigenfrequencies ω for (a) no damping ($r = 0$) and (b) damping with $r = 1.25 \text{ day}^{-1}$; (c) shows contours of power spectrum density of the meridional wind for the stochastic excitation of all wavenumbers (contour interval $10 \text{ m}^2 \text{ s}^{-2} \text{ day}$). The baroclinic (barotropic) basic flow is $U_T = 10 \text{ m s}^{-1}$ ($U = 10 \text{ m s}^{-1}$), the fundamental meridional wavenumber is $l_1 = \pi/3400 \text{ km}$, and Rossby radius is $\kappa^{-1} \sim 720 \text{ km}$. The upper abscissa gives the related phase speed.

vorticity
$$(\nabla^2 \psi_{1,3})_t + U_{1,3}(\nabla^2 \psi_{1,3})_x = \mp \frac{f_0}{\Delta p} \omega_2$$

This leads to additional phase relations between a reference and other wave-solutions (say θ and b), $\gamma_{\theta B} = \arctan\{Im(\Theta/B)/Re(\Theta/B)\}$.

(iv) The *mechanism* of baroclinic instability can be interpreted in terms of a positive feedback between the barotropic ψ -wave and baroclinic θ -wave in vertical shear flow U_T (Fig. 9a, b). The upper and lower layer ψ -waves consist of zonally alternating lows and highs with vertical trough and ridge axes. The θ -wave describes zonally alternating mid-level warm-cold anomalies, whose trough axis is tilted vertically by π . These waves interact by their horizontal and vertical advection of vorticity and temperature as follows:

Vorticity advection, $U_{1,3}(\nabla^2 \psi_{1,3})_x$, creates upper and lower level cyclonic vorticity east and west of the respective troughs (Fig. 9c, d). Thus cyclonic vorticity generation, which is induced by the westward tilted θ -wave, leads to an untilted ψ -wave. On the other hand, the vorticity generation by ψ -wave advection supports a θ -wave of opposing vertical tilt. Thus, there is a negative feedback leading to an oscillation such that the upper (lower) layer cyclones move eastward (westward) relative to the mean flow. *Meridional temperature advection*, $\psi_x U_T$, introduces a feedback loop: The barotropic ψ -wave creates a mid-level warming east of its vertical trough axis which, due to hydrostasy, is associated with an eastern upper level high and lower level low; west of the axis, cooling has the opposing effect (Fig. 9e, f). This induces a westward tilted trough supporting the θ -wave which, due to its vorticity generation, feeds back onto the untilted ψ -wave. Thus the feedback loop is closed and wave amplitudes can grow so that instability arises. However, the instability is diminished by the ψ -wave induced vorticity changes,

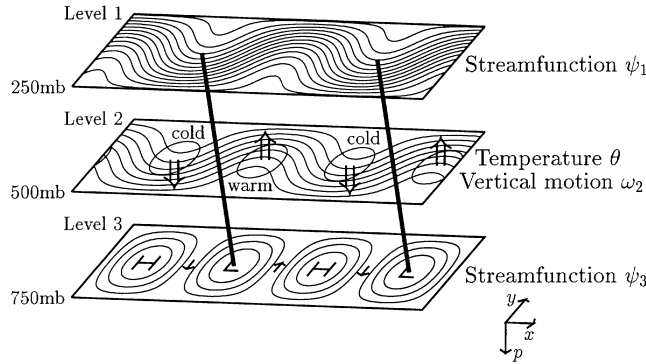


FIGURE 8. Properties of the most unstable Eady-type wave in uniform shear flow in a uniformly rotating environment. The solution depends on x , y , and the pressure level; the trough axis is indicated by a thick line, arrows in mid-level denote vertical velocities. The external parameters U , U_T , l_1 , κ are as in Fig. 7. The basic state streamfunction, $-2U_T y$, is added to level 1.

which do not support the θ -wave tilt and the associated temperature tendencies. *Vertical motion* plays the following role: The advective tendencies caused by the ψ -wave induce non-geostrophy, because pressure and vorticity fields become out of balance. This is compensated by vertical motion (see ω -equation). It counteracts the advective tendencies but cannot cancel them and, therefore, creates a negative feedback (-). Note that the generation of ψ -wave vorticity by vorticity and the generation by temperature advection cancel each other exactly. Therefore, vorticity stretching must dominate over vertical temperature advection in order to have a positive feedback. The first is more influential for long waves ($\sim k$) while the latter dominates for short waves ($\sim k^3$). Thus, positive feedback and instability emerge for longer waves. Shorter waves, however, show oscillating behaviour (short wave cut-off) with uncoupled upper and lower layer dynamics being dominated by the vorticity advection process (no feedback).

(v) *Damping* at top and bottom changes the dispersion relation whose eigenvalues are displayed in the (ω, k) -diagram (Fig. 7b):

$$\text{dispersion } \omega - Uk = -\{ir(K^2 + \kappa^2) \pm i\sqrt{(U_T k)^2(4\kappa^4 - K^4) + r^2\kappa^4}\}/(K^2 + 2\kappa^2)$$

$$\text{instability } (U_T k)^2(4\kappa^4 - K^4) + r^2\kappa^4 > r^2(K^2 + \kappa^2)^2$$

The real parts are comparable with the no damping case. Although the imaginary parts show the stabilizing effect of damping, the maximum instability (no damping) and minimum stability (damping) occur at similar wavenumbers. There is a marginal instability shear in the damped case, $U_{Tm} = rKk^{-1}(2\kappa^2 - K^2)^{-1}$, whose minimum with respect to the zonal wavenumber defines a critical value for instability to occur. The upper and lower layer phase speed occurs at the bifurcation, $U_{Tb} = -r\kappa^2 k_b^{-1}(K_b^4 - 4\kappa^4)^{-1/2}$, whose wavenumber depends on the basic state shear.

(vi) *Perturbation energetics* give an additional description of baroclinic instability. It is obtained by the sum of the barotropic and baroclinic equations after multiplying (3.4) with $-(\psi, \theta)$, respectively, and channel integration, that is summing over all relevant wavenumbers, $[\] = \sum_{K=0}^{K_b}$. Only waves which couple upper and lower layers are associated with meridional heat transport and baroclinic energy conversions. This leads to the channel averaged generation of eddy kinetic and available potential energy, a conversion between the available potential energy reservoirs of the basic state to the eddies, and, finally, the dissipation of kinetic energy D:

$$\text{energetics } [(\psi_x^2 + \psi_y^2) + (\theta_x^2 + \theta_y^2) + 2\kappa^2\theta^2]_t + 4U_T[\kappa^2\psi_x\theta] = D + [\psi\epsilon_\psi + \Theta\epsilon_\theta]$$

Without the stochastic vorticity injection rate ϵ and the associated energy generation, $[\psi\epsilon_\psi + \theta\epsilon_\theta]$, the eddy perturbations gain from the basic-state reservoir of available potential energy, $AZ = [2\kappa^2U_T^2y^2]$, which is represented by the basic state meridional temperature gradient (or U_T) and maintained by the differential heating between polar and tropical regions. The associated basic state

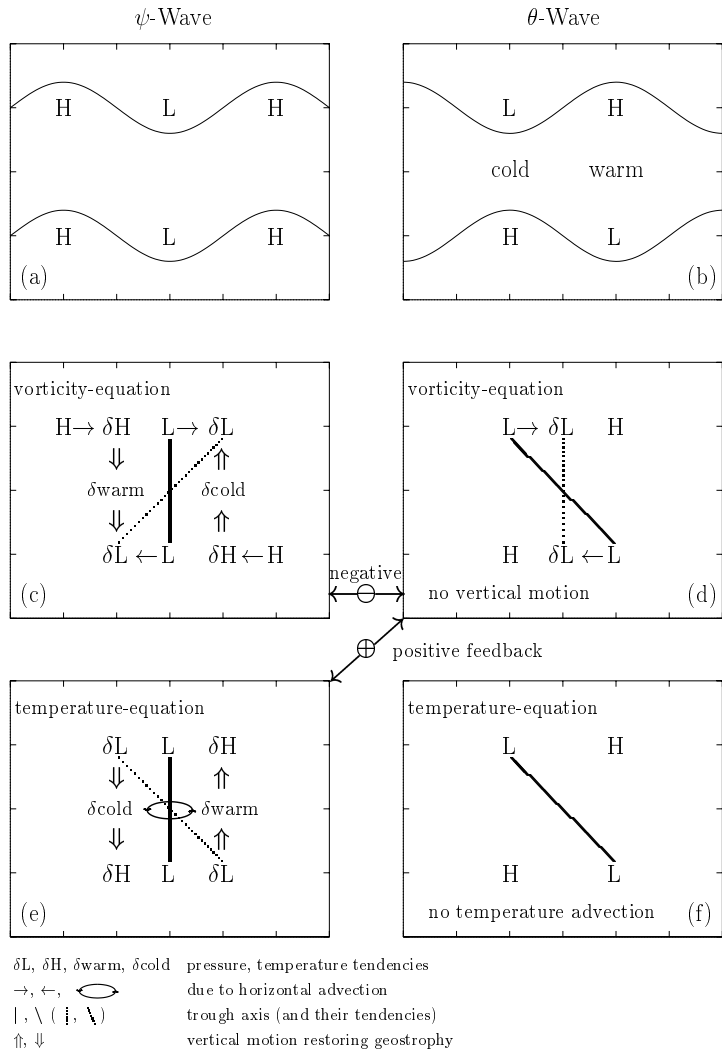


FIGURE 9. Mechanism of baroclinic instability: Zonal cross-section of the ψ - and θ -waves (a, b) and their tendencies induced by the vorticity (c, d) and temperature (e, f) equation. Horizontal vorticity and temperature advections lead to changes of the trough axes ($|, \setminus$) and ageostrophy. Vertical motions tend to restore geostrophy adjusting the vorticity and height changes (and vice versa). A positive feedback links cooperating tendencies (+). The short wave cut-off occurs if the negative feedback ($\sim k^3$) dominates over the positive feedback ($\sim k$) for large wavenumbers (or short waves).

kinetic energy is $KZ = \frac{1}{2}[U_1^2 + U_3^2]$. The baroclinic conversion, $C(AZ, AE) = -4U_T[\kappa^2\psi_x\theta] = U_Tk[\Psi_r\Theta_i - \Psi_i\Theta_r]\kappa^2$, describes the meridional eddy heat flux, $[2\psi_x\theta]$, and its correlation with the meridional temperature gradient (or thermal wind, U_T). It supports the eddy available potential energy reservoir $AE = 2\kappa^2[\theta^2]$ at the expense of the AZ-reservoir, which is constant and, therefore, infinitely large in the linear system. The conversion from AE to eddy kinetic energy, $C(AE, KE) = -\frac{f_o}{\Delta p}[2\omega_2\theta]$, describes vertical overturning by slantwise convection and correlates an upward mid-level vertical massflux ω_2 with a positive temperature (or thickness) anomaly, $f_o\theta$. Finally, the eddy kinetic energy reservoir, $KE = \frac{1}{2}[v_1^2 + v_3^2 + u_1^2 + u_3^2] = \frac{1}{4}[\Psi_r^2 + \Psi_i^2 + \Theta_r^2 + \Theta_i^2]K^2$, is depleted by damping (or dissipation), $D = -2r[\psi_x^2 + \psi_y^2] - 2r[\theta_x^2 + \theta_y^2] = 2rKE$, which closes the linear baroclinic branch of the quasi-geostrophic version of the *Lorenz energy cycle* (for more details see, for example, James' textbook [15]). After suitable seasonal or annual averaging, the energy cycle is a useful diagnostic tool for model simulations and observations; it does not explain cause and effect but keeps balances (baroclinic branch in bold letters):

$$\begin{aligned} \text{Lorenz energy cycle} & \Rightarrow \mathbf{AZ} \Leftarrow C(\mathbf{AZ}, \mathbf{KZ}) \Rightarrow \mathbf{KZ} \Rightarrow D(\mathbf{KZ}) \\ & \quad \Downarrow C(\mathbf{AZ}, \mathbf{AE}) \quad \quad \quad \Uparrow C(\mathbf{KZ}, \mathbf{KE}) \\ & \quad \mathbf{AE} \Rightarrow C(\mathbf{AE}, \mathbf{KE}) \Rightarrow \mathbf{KE} \Rightarrow \mathbf{D}(\mathbf{KE}) \end{aligned}$$

3.3.2. STOCHASTIC ANALYSIS: Maintaining eddy variability against damping requires forcing. It is provided by random vorticity injections which, added to the barotropic and baroclinic mode, leads to the Langevin approach (see DelSole and Farrell [3] for details). Formally, the white noise forcing $\epsilon(t)$ is delta-correlated, $\langle \epsilon_{kl}(t)\epsilon_{kl}^H(t+s) \rangle = q_{kl}\delta(s)$, and, in the frequency domain, $\epsilon(\omega)$, is represented by the intensity matrix, $\langle \epsilon_{kl}(\omega)\epsilon_{kl}^H(\omega) \rangle = \mathbf{Q} = q_{kl}\mathbf{I}$. The wavenumbers excited imply independent forcing of the barotropic and the baroclinic modes by identical magnitudes of vorticity injection through Ekman pumping, $q_{kl} = \text{const}$, of all long waves below the bifurcation value, $K \leq K_b$. The asymptotic spectral response $\mathbf{C}(\omega, k, l)$ can now be determined analytically whose trace defines the variance spectrum $S_{\Phi\Phi}$:

$$\begin{aligned} \text{Langevin weather} & \quad \mathbf{L}\Phi_t = \mathbf{J}\Phi + \epsilon & (3.7) \\ \text{response co-spectra} & \quad \mathbf{C}(\omega, k, l) = (2\pi)^{-1}(\mathbf{J} + i\omega\mathbf{L})^{-1}\mathbf{Q}^H(\mathbf{J}^H - i\omega\mathbf{L}^H)^{-1} \\ \text{variance spectrum} & \quad S_{\Phi\Phi} = q_{kl}N/M \end{aligned}$$

Integration over all frequencies, $\langle \rangle$, gives the total variance at integer wavenumbers, which can be derived by residue calculus (see also DelSole and Farrell [3]). The geopotential height or the meridional geostrophic wind are obtained multiplying with f_o^2 or $k^2f_o^2$, respectively; the kinetic energy is $\frac{1}{2}[K^2 \langle S_{\Phi\Phi} \rangle]$. Analogously, the off-diagonal elements lead to the co-spectrum, $S_{\psi\theta}$, from which the meridional heat flux, $\langle kS_{\psi\theta} \rangle$, can be deduced.

Atmospheric response: The determinant of the matrices attached to the co-spectrum (when deducing their inverse) leads to the numerator N and the denominator $M = \det(\mathbf{J} + i\omega\mathbf{L})\det(\mathbf{J}^H + i\omega\mathbf{L}^H) = \{K^2(K^2 + 2\kappa^2)\}^2(\omega - \omega_1)(\omega - \omega_2)(\omega - \omega_1^H)(\omega - \omega_2^H)$, which contains the squared product of the differences between the driving and the eigenfrequencies, ω and $\omega_{1,2}$:

$$N = (\omega - Uk)^2 \{K^4 + (K^2 + 2\kappa^2)^2\} + (U_T k)^2 (K^4 + (K^2 - 2\kappa^2)^2 + 2r^2 K^4)$$

$$M = \{K^2(K^2 + 2\kappa^2)\}^2 \{(\omega - \text{Re}(\omega_1))^2 + \text{Im}^2(\omega_1)\} \{(\omega - \text{Re}(\omega_2))^2 + \text{Im}^2(\omega_2)\}$$

In the frequency-wavenumber or (ω, k) -domain, the variance density peak occurs at the wavenumber associated with minimum damping (Fig. 7b and c). Further results are noted: (i) The variance spectrum attains a red noise profile, $S_{\Phi\Phi} \sim \omega^{-2}$ for $\omega \rightarrow \infty$. (ii) Location and intensity of the spectral peaks depends sensitively on the choice of the parameters of the model. They identify wavenumber and frequency of the dominant scale of variability responding on the stochastic forcing; the associated zonal phase speed, $c = \omega/k$, is the line connecting peak and origin. (iii) Qualitatively, there is surprisingly good agreement with the southern hemisphere 500 hPa geopotential height observations along 50° South (Fig. 10) which are better represented by a flat zonal channel than the 50° North equivalent, where stationary waves induced by mountains play a prominent role. Note that the magnitude of the response remains to be determined by the intensity of the stochastic forcing, q_{kl} . It is assumed constant for all those wavenumbers which contribute to the meridional heat-flux when upper and lower layers are coupled, $K \leq K_b$.

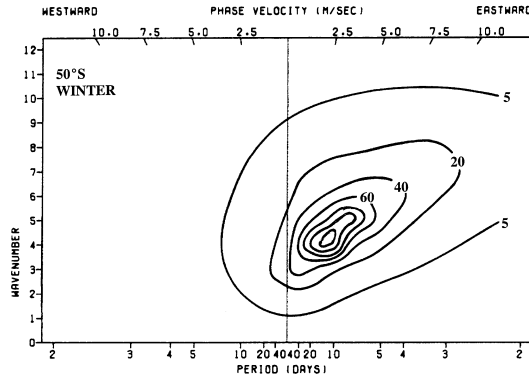


FIGURE 10. Frequency-wavenumber diagram (along 50°South, after Fraedrich and Kietzig [9]): Contours of power spectrum density (in $m^2 s^{-2} day$) of the observed meridional geostrophic wind at 500 hPa in winter. The linear frequency axis is labeled in period (days); the upper abscissa gives the related phase speed (see Fig. 7c).

Closure by entropy balance: The stochastic forcing of the mid-latitude atmosphere is limited by global energy and entropy constraints satisfying both the dynamical and stochastic part of the system. The global entropy balance of the mid-latitude atmosphere leads to a first order closure for the stochastic forcing intensity, q_{kl} , utilising heat exchange between equator and pole as a thermodynamic engine. At equilibrium its efficiency, $\eta = \Delta_y T / T_{in} \sim 10\%$, is a measure of the portion of the total energy input, $R_{in} \sim 100 W m^{-2}$ at subtropical temperatures T_{in} , which is converted by damping, $\langle D \rangle = 2r \langle KE \rangle = \eta R_{in}$. The energy output, $R_{out} = R_{in}$, occurs at subpolar temperatures T_{out} , with $\Delta_y T = T_{in} - T_{out} \sim 25 K$. The efficiency converting the heat input into mechanical energy leads to the asymptotic eddy kinetic energy response of the channel, $\langle KE \rangle \sim 3.5 \cdot 10^5 J m^{-2}$, dissipated at the rate $2r$. Thus the closure, which determines the random injection rate q_{kl} , is prescribed by the system's basic state temperature and radiation field:

$$\text{closure} \quad \langle D \rangle = q_{kl} r [K^2 \langle \frac{N}{M} \rangle] \frac{\Delta p}{g} = \eta R_{in} \quad (3.8)$$

Again, $[] = \sum_{K=0}^{K_b}$ indicates summation over the relevant integer wavenumbers, $K^2 = (k^2 + l_1^2) \leq K_b$ at fixed $l = l_1$, which yields the channel mean. Now, the intensity of the random vorticity injection rate, $q_{kl} \sim 0.8 \cdot 10^{-15} s^{-3}$, can be derived employing residue calculus (see also DelSole and Farrel [3]): $\langle \frac{N}{M} \rangle = \frac{A}{B} + \frac{C}{D}$ with $A = \{K^4 + (K^2 + 2\lambda^2)^2\}$, $B = K^4(K^2 + 2\lambda^2)(K^2 + \lambda^2)$, $C = \{2 + k^2 U_T^2(1 - 4\lambda^2 K^{-2} + 4\lambda^4 K^{-4})r^{-2}\}$, and $D = \{K^2 + k^2 U_T^2(2\lambda^2 - K^2)r^{-2}\}(K^2 + \lambda^2)$.

The closure quantifies the frequency-wavenumber or variance spectrum (3.7). Both structure and magnitude of the variability (Fig. 7c) are surprisingly similar to observations from the 'roaring forties' driving the Southern Ocean (Fig. 10). This response of the stochastically forced linear atmosphere will, in a conceptual sense, enter the following nonlinear ocean model in terms of the spatially inhomogenous stochastic wind forcing of the double gyre.

4. Reduced gravity ocean in a square basin

Prototypes for the study of the mid-latitude wind-driven ocean circulation are the single and double-gyre models in a rectangular basin. They are designed as conceptual tools to study physical mechanisms and hardly used to simulate the actual ocean circulation. The solutions depend sensitively on boundary conditions and subgrid scale parameterisations which are poorly known from observations. Therefore, one of the main tasks of the wind-driven single and double-gyre is to explore the role of dissipative processes within the western boundary currents (for a review see Pedlosky [24]). The role played by dissipative processes to balance the continuous input of vorticity by the wind stress is not the only fundamental problem analysed by the wind-driven gyre models. Their rich structure of multiple equilibria is becoming evident. In particular, the dynamics of the double gyre flow

has received considerable attention as a conceptual model for the North Atlantic current system.

4.1. Shallow-water equations and two-layer model

The two-dimensional shallow water equations govern the motion of a single homogeneous incompressible fluid layer in hydrostatic equilibrium on a rotating sphere, whose depth is small compared to the earth's radius. They can be derived from the three-dimensional momentum equations by vertically integrating the hydrostatic equation with constant density. By including a wind forcing, these equations describe a simple approximation to the depth averaged dynamics of the wind-driven ocean circulation.

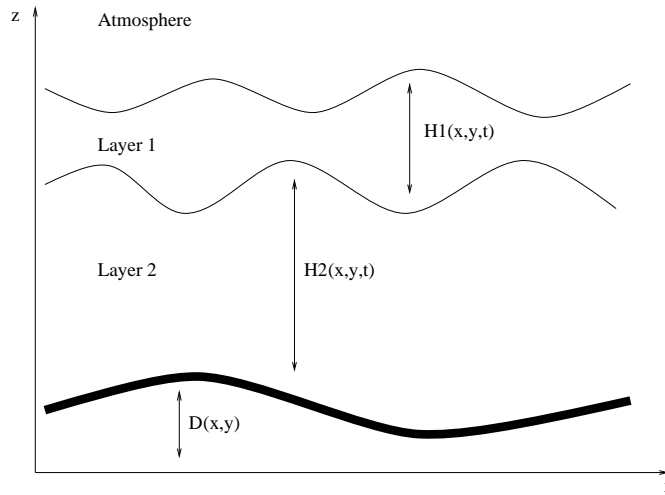


FIGURE 11. Geometry of the two-layer shallow water model.

Derivation of the reduced gravity equations requires introduction of the a two-layer version of the shallow water equations. Consider the motion of two homogeneous layers of uniform but distinct densities shown in Fig. 11. Subscripts 1 and 2 indicate upper and lower layer, respectively, which are attached to the horizontal velocity $\mathbf{u} = (u, v)$, the density ρ , and layer thickness H . The pressure and, therefore, the horizontal pressure gradients in each layer can be calculated by integrating the hydrostatic equation with the surface condition of constant pressure and using continuity of pressure at the interface of the layers with:

$$\begin{array}{ll} \text{layer 1} & \frac{d}{dt} \mathbf{u}_1 + f \mathbf{k} \times \mathbf{u}_1 = -g \nabla H + \mathbf{F}_1 & \frac{dH_1}{dt} = -H_1 \nabla \cdot \mathbf{u}_1 \\ \text{layer 2} & \frac{d}{dt} \mathbf{u}_2 + f \mathbf{k} \times \mathbf{u}_2 = -g \nabla H + g' \nabla H_1 + \mathbf{F}_2 & \frac{dH_2}{dt} = -H_2 \nabla \cdot \mathbf{u}_2 \end{array}$$

The reduced gravity is $g' = g(\rho_2 - \rho_1)/\rho_2$, the layer depth is $H = H_1 + H_2 + D$ where D is the bottom topography, and the total derivative for each layer is designated by $d/dt = \partial/\partial t + \mathbf{u} \cdot \nabla$; g is the acceleration of gravity, and f is the Coriolis parameter given by the β -plane approximation, $f = f_o + \beta y$. Forcing and dissipation terms are summarised in \mathbf{F} .

4.2. Reduced gravity model

In any three-dimensional representation of the oceanic or atmospheric circulation the vertical structure can be represented in terms of barotropic and baroclinic modes. For the ocean the time scale of the barotropic mode is about several hours, whereas the time scales of the baroclinic modes are at least several days. This clear separation of the barotropic and baroclinic time scales allow to use the reduced gravity model to represent the wind-driven circulation of the upper layer.

Assuming the lower layer of infinite depth and at rest, $H_2 \gg H_1$ and $\mathbf{u}_2 = 0$, the barotropic mode is filtered out leading to the reduced-gravity model in component form, whereby the subscript '1' for the upper layer is omitted:

$$\begin{aligned} \text{zonal momentum} & \quad \left(\frac{\partial}{\partial t} + \mathbf{u} \cdot \nabla\right)u = -g'H_x + fv + F_x & (4.1) \\ \text{meridional momentum} & \quad \left(\frac{\partial}{\partial t} + \mathbf{u} \cdot \nabla\right)v = -g'H_y - fu + F_y \\ \text{continuity} & \quad \left(\frac{\partial}{\partial t} + \mathbf{u} \cdot \nabla\right)H = -H(u_x + u_y) \end{aligned}$$

Note that the reduced-gravity equations are similar to the shallow-water equations of flat bottom topography, with gravity g being replaced by the reduced-gravity g' . In the subsequent discussion these equations are used to model the upper ocean in a rectangular basin of 2400 km by 2400 km extent; the (x, y) -coordinates increase eastward and northward.

Parameterisations: The external forcing and internal dissipative terms enter the dynamic equation by the components F_x and F_y :

$$\text{damping/friction} \quad F_x = \frac{\tau^x}{\rho} - ru + A\Delta u, \quad F_y = \frac{\tau^y}{\rho} - rv + A\Delta v \quad (4.2)$$

where $\vec{\tau} = (\tau^x, \tau^y)$ defines the wind stress forcing; the interfacial friction is parameterised by Rayleigh friction scaled by $r = 10^{-7} \text{ s}^{-1} \sim 1/100 \text{ days}$ and the lateral viscosity is represented by a Laplacian scaled by $A = 200 \text{ m}^2 \text{ s}^{-1}$, which are standard values for high resolution models. The atmospheric forcing of the ocean by the wind stress consists of a mean field and stochastic field:

$$\text{wind stress} \quad \vec{\tau} = \vec{\tau}_{mean} + \vec{\tau}_{stochastic}$$

The mean wind stress $\vec{\tau}_{mean}$ is represented by a zonal wind field of a sinusoidal pattern in $-\frac{1}{2}L_y \leq y \leq \frac{1}{2}L_y$ generating a northern cyclonic subpolar and a southern anticyclonic subtropical gyre. The mean or reference wind stress amplitude τ_o is set to a standard value of 0.05 Nm^{-2} . The amplitude of the fluid motion and hence the nonlinearity of the system is proportional to its strength:

$$\tau_{mean}^x \sim \tau_o \cos\left(\frac{2\pi y}{L_y}\right)$$

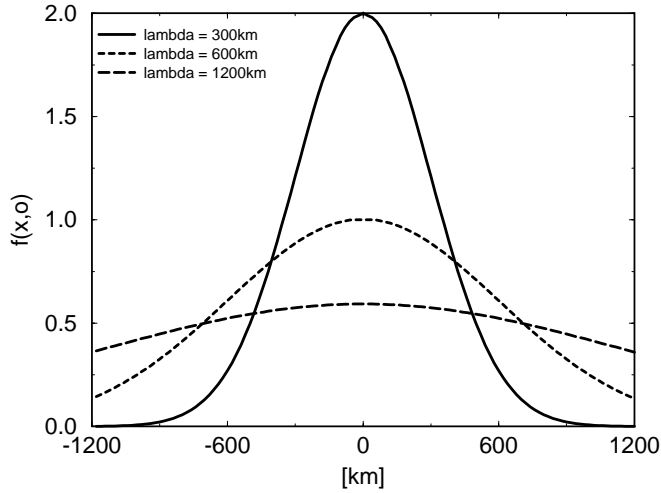


FIGURE 12. The weight function $f(x, y)$ for different values of the inhomogeneity parameter (λ in km) at $y = 0$.

The spatially inhomogeneous stochastic forcing $\vec{\tau}_{stochastic}$ accounts for the high-frequency atmospheric variability and is parameterised by the bulk formula for the wind stress. The bulk formula is used in all experiments, which leads to the parameterisation of the spatially inhomogeneous stochastic forcing:

$$\vec{\tau}_{stochastic} = -\rho_{air} C_D |\mathbf{u}'| \mathbf{u}',$$

where $(u', v') \sim (\epsilon_u(t), \epsilon_v(t)) f(x, y)$, ρ_{air} , $|\mathbf{u}'|$ and \mathbf{u}' are the air density of 1.3 kgm^{-3} , the near surface wind speed and the velocity; $C_D \sim 2 \cdot 10^{-3}$ is the drag coefficient and $\epsilon_{u,v}(t)$ is white noise with zero mean and standard deviation σ . In the numerical experiments the white noise is updated once a day. The weight function $f(x, y)$ parameterizes the spatial structure of the atmospheric variability by a Gaussian shape, whose origin is placed in the center of the basin: $f(x, y) \sim \exp\left(-\frac{x^2}{2\lambda_x^2} - \frac{y^2}{2\lambda_y^2}\right)$. Circular symmetry of the stochastic forcing, $\lambda_x = \lambda_y = \lambda$, is employed for convenience to parameterize the localised atmospheric eddy activity along the storm tracks. The shapes associated with different λ -values used in the numerical experiments are shown in Fig. 12. The variance σ^2 of the white noise is $28 \text{ m}^2 \text{ s}^{-2}$, characterizing the observed atmospheric conditions in the North Atlantic region. This parameterisation is justified by the observed horizontal structure of wind speed standard deviations (see e.g. the COADS data prepared by Wright [34]). For all parameters standard numerical values are used. Furthermore, a standard finite-difference scheme is used to numerically solve the equations with a partial-slip boundary condition (see Sura et al. [30] for details of the numerical scheme and the boundary conditions).

4.3. Analysis of numerical experiments: Design, results, and interpretation

The experiments focus on the nonlinear behaviour of the wind-driven double-gyre circulation in the presence of a spatially inhomogeneous stochastic forcing. Therefore, the model dynamics is analysed by numerical experiments.

Design: The effect of the stochastic wind stress is analysed by four different experiments, three of which are conducted with varying inhomogeneity parameter $\lambda = 300, 600,$ and 1200 km; in addition, a corresponding run without stochastic forcing is performed. In the subsequent discussion only the experiments with $\lambda = 300$ km and the run without stochastic forcing are shown. The experiments commence from a resting state and are integrated for 210 years. The spin-up phase of about 10 years is skipped. For all further diagnostics monthly means are used to calculate the basin integrated eddy kinetic energies (see below) because it is reasonable to employ the period of the non-dispersive first baroclinic Rossby mode in mid-latitudes as an appropriate time scale, which has the order of years. A convenient overall description of the transient behaviour of the basin circulation can be given in terms of the integrated eddy energy content in the basin domain. Therefore, the time series of the basin integrated eddy kinetic and eddy available potential energies are analysed:

$$\text{energy} \quad KE(t) = \frac{1}{2} \rho_1 [\overline{H}(u^2 + v^2)] \quad PE(t) = \frac{1}{2} g' \rho_1 [h'^2] \quad (4.3)$$

where horizontal averaging over the basin domain is denoted by brackets. The layer thickness H is the sum of the equilibrium depth H_o and the depth anomaly h , so that $H(x, y, t) = H_o + h(x, y, t)$. All time dependent variables ψ are separated into a long term mean $\overline{\psi}$ and a deviation ψ' , $\psi = \overline{\psi} + \psi'$. Furthermore, the mass transport stream function is used to present the structure of the flow patterns emphasizing the symmetry properties of the double-gyre.

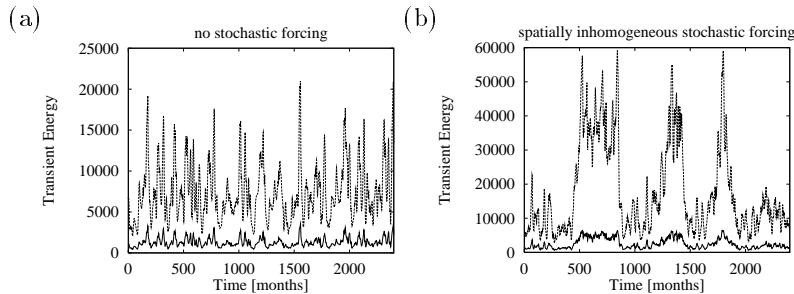


FIGURE 13. Time series of basin integrated eddy energies in Jm^{-2} : a) no stochastic forcing and b) spatially inhomogeneous stochastic forcing ($\lambda = 300$ km). The dashed (solid) line denotes the eddy potential (kinetic) energy.

Results: The double-gyre model with a spatially inhomogeneous stochastic forcing shows a clear bimodal behaviour in the eddy energy time series (see Fig. 13). One regime shows a quasi-antisymmetric, the other regime a nonsymmetric flow pattern (Fig. 14a,b). More details are noted: (i) The nonsymmetric regime equals one member of a well know nonsymmetric pair of stationary solutions. (ii) The nonsymmetric regime does not appear without the spatially inhomogeneous stochastic forcing nor with spatially homogeneous stochastic forcing. Thus, the regime transitions are induced by the spatial inhomogeneity of the white noise variance. (iii) The regime transitions commence from a positive curvature of the jet (Fig. 15). After the transition the system remains in the nonsymmetric regime for several years to decades before the northern extension of the anticyclonic recirculation gyre detaches, again giving rise to the quasi-antisymmetric regime. The residence duration of the nonsymmetric regime depends on the nonlinearity of the system. Thus, the system undergoes a noise-induced transition (Horsthemke et al. [14]), which can occur only if there is a certain amount of randomness in the environment of the system under consideration.

Interpretation: The simple wind-driven ocean model forced by a combination of a double-gyre wind stress and a spatially inhomogeneous stochastic field shows an unexpected bimodal behaviour. One regime is a quasi-antisymmetric state with a free jet penetrating deep into the basin; the more or less strong meandering of the jet does not change the overall flow pattern. The second regime appears to be related to the choice of the spatially inhomogeneous stochastic forcing. It consists of a nonsymmetric flow pattern with a very strong northern recirculation gyre and a north-eastward flowing jet with a penetration scale of 500–600 km. The unexpected result of the presented experimental setup is the appearance of the

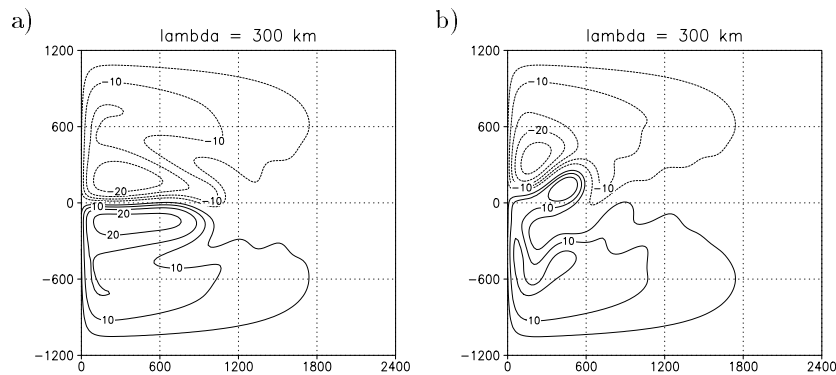


FIGURE 14. Representative mass transport streamfunction fields in $\text{m}^3 \text{s}^{-1}$ for the two different regimes (see Sura et al. [30]): a) low eddy energy state and b) high eddy energy state. The axes are labeled as horizontal distances in km.

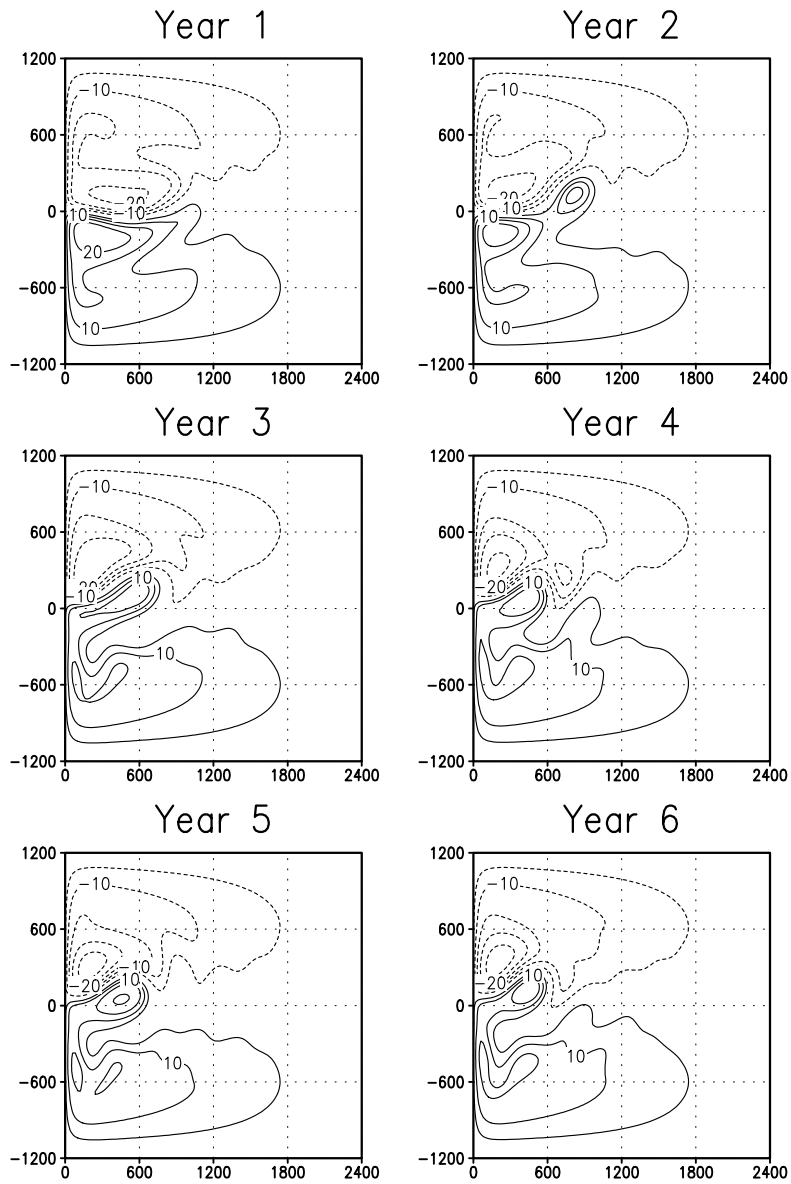


FIGURE 15. Snapshots of representative mass transport stream-function fields (in m^3s^{-1}) with regime transitions (see Sura et al. [30]). The axes are labeled as horizontal distances in km. The origin of the annual sequence is arbitrarily chosen.

nonsymmetric regime in the presence of the spatially inhomogeneous stochastic wind forcing (Fig. 14b). This nonsymmetric regime represents a member of the nonsymmetric part of stationary solutions. This is in agreement with McCalpin et al. [21] who found no evidence of a bimodal behaviour related to multiple equilibria, as long as the pure antisymmetric windforcing is used.

Thus the stochastic forcing enables the system to reach the neighborhood of an unstable fix point, which cannot be reached without the spatially inhomogeneous stochastic wind field. The unstable fixed point then acts to steer the model evolution in a temporarily persistent regime. Transitions into the nonsymmetric regime commence from an abnormally positive curvature of the jet which also cannot be attained without the spatially inhomogeneous stochastic wind stress. That is, the curl of the localised stochastic wind stress forces an anomaly which leads to the abnormal curvature of the jet. Thereby the very small basin of attraction of the nonsymmetric state is reached and initiates the regime transition from the quasi-antisymmetric, low eddy energy state to the nonsymmetric, high eddy energy state. The transition back into the quasi-antisymmetric regime is caused by the detachment of the northern extension of the anticyclonic recirculation gyre.

The behaviour of the wind-driven ocean circulation can be substantially modified by the stochastic forcing of the atmosphere. This emphasizes the important concept of noise-induced regime transitions in the wind-driven circulation. In this sense, the analysis suggests [2] that multiple equilibria are of significance in the description of the low-frequency variability of the wind-driven ocean circulation, regardless of their stability.

5. Summary and outlook

These lecture notes introduce the global climate system and two of its major players: the atmosphere and the ocean. Leitmotif is a toy modelling approach to the analysis and understanding of climate variability in terms of noise and noise induced transitions. First, a minimum climate model is derived to demonstrate the model building strategy from a coupled atmosphere-ocean system to a statistic-dynamical model with a parameterised atmosphere. In addition, analysis methods are presented summarised under the key words stability, sensitivity, and stochasticity. The stability analysis shows how elementary catastrophes describe the topological structure of a zero-dimensional climate system. Sensitivity analysis is a frequently used technique analysing feedbacks in the real world and demonstrating the effect of varying external parameters on the equilibrium state. Additive white noise, which parameterises the influence of the fast atmosphere on the climate, leads to the conventional Langevin approach explaining the variability about the equilibrium as a stochastic response. A closure required to couple the stochastic forcing intensity with the global climate thermodynamics leads to realistic estimates of this variability. Next, atmosphere and ocean are treated. A

textbook toy model explains mid-latitude weather systems by the linear baroclinic instability of a zonal basic state in a quasi-geostrophic channel. A novel interpretation of the baroclinic instability is presented in terms of feedbacks between the barotropic and baroclinic modes. Including damping through Ekman pumping stabilises the system; adding stochastic forcing leads to an asymptotic response (presented in a wavenumber-frequency spectrum) which is in qualitative agreement with the observed variability of the mid-latitude westerlies. Employing a thermodynamic closure leads towards a consistent parameterisation of synoptic scale eddies. Conceptually, this response (or parameterization) serves as a link to the nonlinear ocean toy model which describes the double gyre circulation in a square shallow water basin driven by a mean and stochastic wind forcing field. Sufficient spatial inhomogeneity of the atmosphere's stochastic forcing leads to transitions between two ocean regimes one of which would not occur otherwise. This introduces a new concept of decadal variability in the climate system.

With stochastic forcing being the overall theme, a climate modelling concept emerges. That is, the response of a stochastically forced linear atmosphere serves as a parameterisation of the fast fluctuating mid-latitude eddies which, by the mean and the spatially inhomogeneous eddy wind forcing, drives the slow nonlinear ocean to possible regime transitions. What remains is the introduction of a feedback from the ocean to the atmosphere which, for the mid-latitudes discussed here, is one of the priority research areas.

References

- [1] M.I. Budyko, The effect of solar radiation variations on the climate of the earth, *Tellus*, **21** (1969), 611-619.
- [2] P. Cessi and G.R. Ierley, Symmetry-Breaking multiple equilibria in quasigeostrophic, wind-driven flow, *J. Phys. Oceanogr.*, **25** (1995), 1196-1205.
- [3] T. DelSole and B.F. Farrell, A stochastically excited linear system as a model for quasigeostrophic turbulence: analytic results for one-and two-layer fluids, *J. Atmos. Sci.*, **52** (1995), 2531-2547.
- [4] E. Eliassen and L. Laursen, A seasonal global climate model with an equivalent meridional atmospheric circulation, *Tellus*, **34** (1982), 514-525.
- [5] E.T. Eady, Long waves and cyclone waves, *Tellus*, **1** (1949), 33-52.
- [6] K. Fraedrich, Structural and stochastic analysis of a zero-dimensional climate system, *Q. J. R. Meteorol. Soc.*, **104** (1978), 461-474.
- [7] K. Fraedrich, *Atmospheric variability: modelling, diagnostics, and forecasting*, International School of Physics 'Enrico Fermi' Course CXXXIII 'Past and Present Variability of the Solar-Terrestrial System: Measurements, Data Analysis and Theoretical Models', (G. Cini Castagnoli and A. Provenzale, Eds.) (1997), 431-483.
- [8] K. Fraedrich, Catastrophes and resilience of a zero-dimensional climate system with ice-albedo and greenhouse feedback, *Q. J. R. Meteorol. Soc.*, **89** (1979), 147-167.

- [9] K. Fraedrich and E. Kietzig, Statistical Analysis and wavenumber-frequency spectra of the 500mb geopotential at 50°S, *J. Atmos. Sci.*, **40** (1983), 1037-1045.
- [10] C.W. Gardiner, *Handbook of Stochastic Methods*, Springer-Verlag, (1985), 442pp.
- [11] D.L. Hartmann, *Global Physical Climatology*, Academic Press, (1994), 411pp.
- [12] K. Hasselmann, Stochastic climate models. Part I. Theory, *Tellus*, **28** (1976), 473-484.
- [13] J.R. Holton, *An Introduction to Dynamic Meteorology*, Academic Press, (1992), 511pp.
- [14] W. Horsthemke and R. Lefever, *Noise-Induced transitions: theory and applications in physics, chemistry, and biology*, Springer-Verlag, (1984), 318pp.
- [15] I.N. James, *Introduction to Circulating Atmospheres*, Cambridge University Press, (1994), 422pp.
- [16] E. Källen, C. Craford, and M. Ghil, Free oscillations in a climate model with ice-sheet dynamics, *J. Atmos. Sci.*, **36** (1979), 2292-2303.
- [17] J.E. Kutzbach and R. Bryson, Variance spectrum of holocene climate fluctuations in the North Atlantic sector, *J. Atmos. Sci.*, **31** (1974), 1958-1963.
- [18] P. Lemke, Stochastic climate models, Part 3. Application to zonally averaged energy models, *Tellus*, **29** (1977), 385-392.
- [19] B. Legras and M. Ghil, Persistent anomalies, blocking and variations in atmospheric predictability, *J. Atmos. Sci.*, **42** (1985), 433-471.
- [20] M. Margules, Über die Energie der Stürme, *Jahrbücher KK Zentralanstalt für Meteorologie und Erdmagnetismus*, **NF 40** (1905), 1-26.
- [21] J. McCalpin and D.B. Haidvogel, Phenomenology of the low-frequency variability in a reduced-gravity quasigeostrophic double-gyre model, *J. Phys. Oceanogr.*, **26** (1996), 739-752.
- [22] G.R. North, R.F. Cahalan, and J.A. Coakley, Energy balance climate models, *Rev. Geophys. Space Phys.*, **19** (1981), 91-121.
- [23] J. Pedlosky, *Geophysical Fluid Dynamics*, Springer-Verlag, (1987), 710 pp.
- [24] J. Pedlosky, *Ocean Circulation Theory*, Springer-Verlag, (1996), 453 pp.
- [25] F.W. Primeau, Multiple Equilibria of a double-gyre ocean model with super-slip boundary conditions, *J. Phys. Oceanogr.*, **28** (1998), 2130-2147.
- [26] B. Saltzman, *A survey of statistical-dynamical models of the terrestrial climate*, *Advances in Geophysics*, **20** (1978), 184-304.
- [27] B. Saltzman, A. Sutera, and A. Evenson, Structural stochastic stability of a simple auto-oscillatory climatic feedback system, *J. Atmos. Sci.*, **38** (1981), 494-503.
- [28] B. Saltzman, *Climatic systems analysis. In: Theory of Climate (Ed.: B. Saltzman)*, *Advances in Geophysics*, **25** (1983), 173-233.
- [29] J.-S. von Storch, Complex Climate Models, *Progress in Probability*, Birkhäuser Verlag.
- [30] P. Sura, K. Fraedrich, and F. Lunkeit, Regime transitions in a stochastically forced double-gyre model, *J. Phys. Oceanogr.*, **30** (2000), in press.
- [31] W.C. Swinbank, Long-wave radiation from clear skies, *Q. J. R. Meteorol. Soc.*, **89** (1963), 339-348.

- [32] R. Thom, *Structural stability and morphogenesis*, Benjamin Inc., Reading, Mass. (1975), 347pp.
- [33] R.T. Wetherald and S. Manabe, The effects of changing the solar constant on the climate of a general circulation model, *J. Atmos. Sci.*, **32** (1975), 2044-2059.
- [34] P.B. Wright, *An atlas based on the COADS data set: Fields of mean wind, cloudiness and humidity at the surface of the global ocean*, Max-Planck-Institut für Meteorologie, **14** (1988), 68pp.

Klaus Fraedrich
Meteorologisches Institut
Universität Hamburg
D-20146 Hamburg
Germany
Date 2/9 (HH)
E-mail address: fraedrich@dkrz.de

In "Progress in Probability" (eds. P. Imkeller and J.-S. von Storch),
Birkhäuser Verlag.